bioRxiv preprint doi: https://doi.org/10.1101/2020.02.19.955567; this version posted June 21, 2020. The copyright holder for this preprint (which was not certified by peer review) is the author/funder, who has granted bioRxiv a license to display the preprint in perpetuity. It is made available under aCC-BY-NC-ND 4.0 International license.

A quantitative principle to understand 3D cellular connectivity in epithelial tubes

Pedro Gómez-Gálvez[1,2,†], Pablo Vicente-Munuera[1,2,†], Samira Anbari[3,†], Antonio Tagua[1,2,†], Carmen Gordillo-Vázquez[1,2], Ana M. Palacios[1,2], Antonio Velasco[1], Carlos Capitán-Agudo[1], Clara Grima[5], Valentina Annese[1,2], Rafael Robles[5], Alberto Márquez[5], Javier Buceta[3,4,*], Luis M. Escudero[1,2,*]

1: Instituto de Biomedicina de Sevilla (IBiS), Hospital Universitario Virgen del Rocío/CSIC/Universidad de Sevilla and Departamento de Biología Celular, Universidad de Sevilla. 41013 Seville, Spain.

2: Biomedical Network Research Centre on Neurodegenerative Diseases (CIBERNED), Madrid, Spain.

3: Chemical and Biomolecular Engineering Department, Lehigh University. Bethlehem, PA 18018, USA.

4: Bioengineering Department, Lehigh University. Bethlehem, PA 18018, USA.

5: Departamento de Matemática Aplicada I, Universidad de Sevilla. 41012 Seville, Spain.

†: These authors contributed equally to this work.

*: Corresponding authors

bioRxiv preprint doi: https://doi.org/10.1101/2020.02.19.955567; this version posted June 21, 2020. The copyright holder for this preprint (which was not certified by peer review) is the author/funder, who has granted bioRxiv a license to display the preprint in perpetuity. It is made available under aCC-BY-NC-ND 4.0 International license.

ABSTRACT

Apico-basal cell intercalations (scutoids) optimize packing and energy expenditure in curved epithelia. Further consequences of this new paradigm of tissue packing remain uncharacterized. In particular, how scutoids modify the 3D cellular connectivity is an open question. This property is crucial for understanding epithelial architecture and is instrumental for regulating the biological function of tissues. Here, we address this problem by means of a computational model of epithelial tubes and a biophysical approach that links geometrical descriptors with the energetic cost required to increase the cellular connectivity. Our results predict that epithelial tubes satisfy a novel quantitative principle: the “Flintstones’ law”. In short, cellular connectivity increases with tissue thickness/curvature in a logistic way. We confirm experimentally the existence of this principle using *Drosophila*’s salivary glands. Our study provides methodological advances to analyze tissue packing in 3D and, more importantly, unveils a morphogenetic principle with key biological consequences.

KEYWORDS

Epithelial architecture, Tubulogenesis, Mathematical/Biophysical modeling, Computational geometry, Developmental systems biology, Cellular connectivity.

bioRxiv preprint doi: https://doi.org/10.1101/2020.02.19.955567; this version posted June 21, 2020. The copyright holder for this preprint (which was not certified by peer review) is the author/funder, who has granted bioRxiv a license to display the preprint in perpetuity. It is made available under aCC-BY-NC-ND 4.0 International license.

INTRODUCTION

During the last decades much progress has been achieved in the understanding of the emergence of self-organization in tissues. This problem has been addressed from the viewpoint of energetics considerations (Alt et al., 2017; Canela-Xandri et al., 2011; Fletcher et al., 2014; Misra et al., 2017; Nelson et al., 2005; Siedlik et al., 2017; Sugimura et al., 2016; Trepat et al., 2009), material-like properties (Bi et al., 2015; Campàs et al., 2014; Latorre et al., 2018; Mongera et al., 2018; Pérez-González et al., 2019; Yang et al., 2017), and the analysis of the packing properties. As for the latter, the analysis of epithelial surfaces as tessellations of convex polygons has been successfully used to quantitatively understand different biological aspects such as tissue patterning, cell division, and growth (Box et al., 2019; Curran et al., 2017; Farhadifar et al., 2007; Gibson et al., 2006, 2011; Honda, 1978; Lewis, 1928; Mao et al., 2013; Sánchez-Gutiérrez et al., 2016; Thompson, 1945). Importantly, these studies have also revealed the validity of mathematical principles with biological consequences. One relevant example are the implications of Euler´s formula (Reinhardt, 1918; Wetzel, 1926) about cellular connectivity. This formula implies that polygonal cells in packed tissues, on average, have six neighbors (i.e., the average 2D cellular connectivity reads $\langle n_{2D} \rangle = 6$). As for its biological consequences, the degree of cellular connectivity determines, for example, the strength of the cell-cell juxtracrine signaling (Tung *et al*, 2012; Sharma *et al*, 2019; Perrimon *et al*, 2012). Not surprisingly, the validity of this connectivity principle to the third dimension has been taken for granted since the role played by apico-basal cell intercalations has been disregarded and cells have been assumed to have prismatic-like shapes in either planar or bent epithelia.

However, the recent discovery of more complex cellular geometries in epithelial cells, i.e., scutoids, to reach an efficient three-dimensional (3D) tissue packing has set a new paradigm that has not been yet fully explored (Gómez-Gálvez et al., 2018; Mughal et al., 2018; Rupprecht et al., 2017). Scutoids imply spatial changes in the neighboring relationship between cells (**Fig. 1A**). This phenomenon is then a spatial version of the T1 transitions that produce cell rearrangements with time in numerous developmental processes

bioRxiv preprint doi: https://doi.org/10.1101/2020.02.19.955567; this version posted June 21, 2020. The copyright holder for this preprint (which was not certified by peer review) is the author/funder, who has granted bioRxiv a license to display the preprint in perpetuity. It is made available under aCC-BY-NC-ND 4.0 International license.

(Bertet et al., 2004; Irvine and Wieschaus, 1994; Spencer et al., 2017). Thus, the presence of scutoids necessarily modifies the connectivity and the biophysical properties of tissues. Still, the analysis of tissue organization in a 3D context, and the corresponding biological repercussions, have been hindered by the technical difficulties to accurately segment and reconstruct cells from apical to basal surfaces. In addition, very few computational models account for the presence of apico-basal transitions to investigate 3D self-organization in tissues (Gómez-Gálvez et al., 2018; Mughal et al., 2018; Okuda et al., 2019; Rupprecht et al., 2017).

The realistic analysis of 3D packing is in turn utterly relevant in epithelial tubes, where scutoids appear more frequently (Gómez-Gálvez et al., 2018; Iruela-Arispe and Beitel, 2013; Sanchez-Corrales et al., 2018). Epithelial tubes are in fact the primary developmental structures in all organisms with bilateral symmetry (Gilbert and Barresi, 2016) and tubulogenesis is fundamental in a broad variety of key developmental processes, including gastrulation and neurulation (Colas and Schoenwolf, 2001; Iruela-Arispe and Beitel, 2013; Leptin and Grunewald, 1990; Nelson, 2009; Pilot and Lecuit, 2005; Swanson and Beitel, 2006). Furthermore, epithelial tubes are the essential functional unit of many mammalian organs, including glands, components of the digestive apparatus, lungs, and kidney (Huebner and Ewald, 2014). Hence, the faithful formation and function of tubes requires the precise coordination of dynamic changes in the tissue architecture, i.e., packing, during development (Röper, 2018).

Here, we study the packing and the 3D cellular connectivity properties of epithelial tubes. We show that the presence of scutoids implies a breakdown of the principle $\langle n_{3D} \rangle = 6$ and reveal a novel law that quantitatively links the 3D cellular connectivity, geometrical descriptors (e.g., tissue curvature/thickness), and energetics. Our findings are supported by i) a computational model that realistically render the 3D cellular organization of tubular epithelia (including the appearance of scutoids); ii) a biophysical model, supported by mathematical calculations, that connects the tissue energetics with the 3D organization of epithelial tubes; and iii) experimental data of epithelial tubes

bioRxiv preprint doi: https://doi.org/10.1101/2020.02.19.955567; this version posted June 21, 2020. The copyright holder for this preprint (which was not certified by peer review) is the author/funder, who has granted bioRxiv a license to display the preprint in perpetuity. It is made available under aCC-BY-NC-ND 4.0 International license.

(*Drosophila*'s salivary gland) whose 3D cellular structure has been accurately characterized by means of a novel computer-aided image analysis method.

Altogether, by realistically capturing the organization of cells in tubular epithelia, we shed light on the important issue of how tissues are 3D shaped and we open the door to understand quantitatively key morphogenetic events that ultimately depends on the 3D cellular connectivity.

RESULTS

A computational model unveils the connectivity properties of tubular epithelia

To understand how the geometry of tubular epithelia affects the 3D cellular packing and connectivity, we designed and implemented a computational Voronoi tubular model (Gómez-Gálvez et al., 2018) (**Materials and Methods**). We analyzed tubes with an increasing surface ratio (radial expansion), $s_b = R_b/R_a$ (**Fig. 1B**). This parameter quantifies the ratio of the non-trivial curvatures of apical and basal tubular surfaces, $\kappa_a/\kappa_b = R_b/R_a = s_b$, and it is a proxy for the dimensionless tissue thickness, $(R_b - R_a)/R_a = (s_b - 1)$. In addition, we explored the cellular organization of tubes by using a Centroidal Voronoi Tessellation (CVT) scale (**Fig. 1C**). The CVT scale accounts for the number of iterations of the homogenizing Lloyd's algorithm and makes possible to analyze the effect of the topological order of the tissue (**Materials and Methods**) (Gómez-Gálvez et al., 2018; Sánchez-Gutiérrez et al., 2016).

Our results showed that the average number of apico-basal intercalations per cell, $\langle i(s_b)\rangle$, (**Fig. 1D**), and therefore the percentage of cells adopting the scutoidal shape (**Fig. S1**), increases with s_b and decreases as tubes become more ordered (i.e., as the CVT index increases). To further uncover the 3D organization of tissues, we implemented a benchmark able to reveal simultaneously the existence of apico-basal intercalations (scutoids) and the polygonal distributions of cells. To that end, we computed the probability that cells change their polygonal class between the apical and basal surfaces. Thus, the components (i.e., bins) of this distribution along the diagonal account for prismatic cells (**Fig. 2A**) whereas the spreading away from the diagonal reveals the existence of scutoids (cells that exchange neighbors due

bioRxiv preprint doi: https://doi.org/10.1101/2020.02.19.955567; this version posted June 21, 2020. The copyright holder for this preprint (which was not certified by peer review) is the author/funder, who has granted bioRxiv a license to display the preprint in perpetuity. It is made available under aCC-BY-NC-ND 4.0 International license.

to apico-basal intercalations) and, consequently, changes in the cellular 3D connectivity in the tissue (**Fig. 2B**). In agreement with the results shown in **Fig. 1D**, our data indicates that the degree of spreading of the distribution (as quantified by the parameter, η^2, **Materials and Methods**) increases with the surface ratio and decreases when the initial (i.e., apical) Voronoi diagram became more ordered, that is, as the CVT increases (**Fig. 2C**).

Moreover, we computed the average of the total number of contacts of the cells, $\langle n_{3D} \rangle$, as a function of the surface ratio and the initial Voronoi diagram (**Fig. 2D**). Our data are quantitatively consistent with a mathematical derivation that shows that $\langle n_{3D} \rangle$ is linearly proportional to the number of apico-basal intercalations (**Materials and Methods** and **Fig. S1**). Also, these results indicated that the average cellular connectivity grows as the tissue thickness and the randomness of cellular organization increases.

In summary, our computational model suggests a relation between the tissue geometry (i.e., cell thickness/curvature), the cellular planar topological order (CVT index), and the 3D cellular connectivity in epithelial tubes.

The 3D neighbor's accumulation follows a "poor get richer" principle

In order to shed light on the underlying mechanisms that determine the degree of 3D cellular connectivity in our model of tubular epithelia, we computed the net gain of cellular neighbors as a function of the radial expansion (thickness/curvature of tubes) and the topological properties of cells (CVT index and polygonal class at the apical surface). As a general trend, we observed that, independently of the radial expansion, the smaller the number of neighbors at the apical surface the larger the net gain of 3D cellular contacts (**Fig. 3A and B** and **Fig. S2**). Additionally, we also checked that this tendency is satisfied when estimating the net gain of neighbors accumulated from the basal to the apical surface (**Fig. S2**). These results suggest that in the Voronoi tubular model the 3D cell packing follows a "poor get richer" principle driven by apico-basal intercalations: the less neighbors a cell has in a surface (apical or basal), the larger the net increase of cellular contacts. Interestingly, this result is akin to the behavior found in planar geometries that indicates that

bioRxiv preprint doi: https://doi.org/10.1101/2020.02.19.955567; this version posted June 21, 2020. The copyright holder for this preprint (which was not certified by peer review) is the author/funder, who has granted bioRxiv a license to display the preprint in perpetuity. It is made available under aCC-BY-NC-ND 4.0 International license.

the probability of undergoing a T1 transition increases as the number of neighbors decreases (Bi et al., 2014), see Discussion.

An energetics model suggests that cellular connectivity satisfies a logistic-like law

In light of this evidence, and in order to better understand the dependence of the tissue self-organization on the radial expansion, $s = R/R_a$, we developed a biophysical model (a Kolmogorov rate equation) that accounts for the probability of cells to increase their 3D connectivity (**Fig. 4A and B** and **Materials and Methods**):

$$\frac{dP_m(s)}{ds} = P_{m-1}(s)r_{m-1,m} - P_m(s)r_{m,m+1} \quad (1)$$

where, P_m, is the probability of having m accumulated 3D neighbors (i.e., $m = n_{3D}$) as the surface ratio changes from s to $s + ds$, and $r_{i,i+1}$ accounts for the rate per unit of surface ratio of undergoing an apico-basal intercalation. By drawing parallels between apico-basal intercalations and planar T1 transitions (Gómez-Gálvez et al., 2018; Sanchez-Corrales et al., 2018) we assumed that cells need to overcome an energy barrier to gain a 3D neighbor, that is, $r_{i,i+1} \sim e^{-\Delta E_i}$ (**Fig. 4A and B**). The "poor get richer" principle suggests that ΔE_i grows as i increases. In addition, our mathematical calculations proved that the apico-basal intercalation rate becomes null for a finite value of i (**Box** and **Materials and Methods**): neighbors' gaining is necessarily bounded or, energetically speaking, the energy barrier to undergo an apico-basal transition becomes eventually infinite. All these facts led to the following expression for the apico-basal intercalation rate: $r_{i,i+1} = \alpha(N_{max} - i)e^{-i\beta}$, where α is a 'bare' transition rate, β is the dimensionless energy (in units of the four-fold vertex energy configuration) per 3D neighbor that a cell needs to increase its connectivity to an additional cell, and N_{max} is the maximum 3D cellular connectivity (**Materials and Methods**).

The fitting of the *in silico* data about the average tissue connectivity, $\langle n_{3D}(s)\rangle = \sum_m m\, P_m(s)$, to this biophysical model showed an excellent agreement and confirmed that $\langle n_{3D}\rangle > 6$ as long as the tissue is subjected to some level of anisotropic curvature (**Fig. 4C, Fig. S3** and **Materials and Methods**). We also observed that the energy required per 3D neighbor to

bioRxiv preprint doi: https://doi.org/10.1101/2020.02.19.955567; this version posted June 21, 2020. The copyright holder for this preprint (which was not certified by peer review) is the author/funder, who has granted bioRxiv a license to display the preprint in perpetuity. It is made available under aCC-BY-NC-ND 4.0 International license.

undergo an intercalation, β, quickly reached a plateau, $\beta \simeq 5 \cdot 10^{-2}$, as the tissue became more ordered (i.e., as the CVT index increases). Our results also indicate that in Voronoi tubes the scutoidal geometry enables a theoretically increase of the average 3D cellular connectivity up to $\langle N_{max} \rangle \sim 12 - 15$ cells (**Table S1**). In addition, the plausibility of the Kolmogorov approach was further assessed by predicting the 3D neighbor distribution, $P_m(s)$, thus confirming that a link between geometrical and energetic traits determines the cellular connectivity in the Voronoi tubular model (**Fig. 4C)**.

We also obtained theoretically an analytical formula that characterizes the average 3D cellular connectivity, $\langle n_{3D} \rangle$ (**Box** and **Materials and Methods**). We concluded that in the Voronoi tubular model $\langle n_{3D} \rangle$ can be described by a logistic-like behavior,

$$\langle n_{3D}(s) \rangle \approx \langle N_{max} \rangle \frac{1+be^{-\frac{s}{c}}}{1+de^{-\frac{s}{c}}}, \quad (2)$$

where b, c, and d are non-independent parameters that are functions of α, β, and $\langle N_{max} \rangle$ (**Table S1** and **Materials and Methods**). We refer to this logistic-like principle as the "Flintstones' law" after the Stone-Age cartoon characters. We argue that this organizing principle is as ancient as the first organized tissue found in evolution: epithelia (hereby the name).

The analysis of computational tubes revealed the validity of the Flintstones' law as an effective way to determine the cellular connectivity in a model of tubular epithelia as a function of the radial expansion (**Fig. 4C** and **Fig. S3**). More importantly, it provides a straightforward way to estimate/predict the value of the underlying energetic properties regulating apico-basal intercalations and the limiting average 3D cellular connectivity (**Table S1**).

Experiments confirm that the 3D cellular connectivity in tubular epithelia satisfies the Flintstones' law

In order to confirm our computational and theoretical predictions, we implemented a novel methodological pipeline that combines several computational image analysis techniques to accurately segment cells of *in vivo* epithelial tubes (Arganda-Carreras et al., 2017; Machado et al., 2019)

bioRxiv preprint doi: https://doi.org/10.1101/2020.02.19.955567; this version posted June 21, 2020. The copyright holder for this preprint (which was not certified by peer review) is the author/funder, who has granted bioRxiv a license to display the preprint in perpetuity. It is made available under aCC-BY-NC-ND 4.0 International license.

(**Materials and Methods**). We used the *Drosophila* larval salivary gland as a model due to its ideal characteristics to study complex tubular architectures (Girdler and Röper, 2014) (**Fig. 5A-C**).

Our methodology allowed to determine the average surface ratio of the salivary glands ($s_b = 4.0 \pm 0.4$), $\langle n_{3D}(s_b)\rangle = 6.7 \pm 0.2$, the average percentage of scutoids ($76 \pm 11\%$), and the average number of apico-basal intercalations per cell, $\langle i(s_b)\rangle = 1.4 \pm 0.4$, thus confirming the validity of the formula that relates apico-basal intercalations per cell and the average connectivity: $\langle n_{3D}\rangle = 6 + \langle i\rangle/2$ (**Materials and Methods** and **Fig. S1**). We also calculated the polygonal class distribution in the apical and basal surfaces (**Fig. S4**). Interestingly, in spite of the prevalence of scutoids, the polygonal organization of apical and basal surfaces was found to be the same and equivalent to that obtained in *in silico* V8 tubes with a radial expansion $s_b = 1.75$ (**Fig. S4**). This V8 model ($s_b = 1.75$) also displayed a similar scutoidal prevalence ($79 \pm 5\%$), average number of 3D neighbors, average number of apico-basal intercalations per cell, and η^2 spreading that *in vivo* tubes (**Fig. 5D** and **Fig. S4**). We additionally confirmed that the apical and basal surfaces of the V8 model and the salivary glands fulfilled, as expected, that $\langle n_{2D}\rangle \approx 6$ (Reinhardt, 1918; Wetzel, 1926) (**Fig. S4**). Thus, we concluded that the *in silico* V8 model with a radial expansion of $s_b = 1.75$ faithfully recapitulates the 3D packing properties of *in vivo* salivary glands.

As for the 3D cellular connectivity of *in vivo* tubes, our analyses confirmed that the "poor get richer" principle was satisfied, thus supporting the idea that the smaller the number of neighbors of a cell in a surface, the larger the probability to increase its connectivity (**Fig. S4**). Additionally, by implementing an un-rolling (i.e., peel-off) algorithm (Yang et al., 2019) (**Materials and Methods**), we obtained concentric radial sections and quantified the number of 3D neighbors as a function of the radial expansion. The fitting of the data to the Kolmogorov model showed an excellent agreement and allowed to estimate the energetic properties as summarized by the parameter β (**Fig. 5E** and **Table S1**). Our results suggested that the energy per 3D cell required to undergo an apico-basal intercalation is larger in *in vivo* tubes than in the computational V8 model, see Discussion. Importantly, the 3D cellular

bioRxiv preprint doi: https://doi.org/10.1101/2020.02.19.955567; this version posted June 21, 2020. The copyright holder for this preprint (which was not certified by peer review) is the author/funder, who has granted bioRxiv a license to display the preprint in perpetuity. It is made available under aCC-BY-NC-ND 4.0 International license.

connectivity data confirmed the applicability of the Flintstones' law in *in vivo* tubular epithelia (**Fig. 5E** and **Table S1**).

DISCUSSION

Here we have shown how mathematical and physical principles underlie the emergence of functionally complex 3D developmental structures, e.g., glands. Our analyses have uncovered for the first time how a 2D organizational trait, i.e., the cellular connectivity, can be extended to the third spatial dimension when the novel paradigm of epithelial cells' shapes and packing, the scutoid, is considered. In that regard, we have revealed how the 3D cellular connectivity and tissue energetics are coupled, and we have stated a novel principle, the so-called Flintstones' law. The latter links the activation energy needed to recruit additional neighbors with geometrical descriptors (i.e., tissue thickness/curvature). Our results provide new biological insight into the spatiotemporal regulation of cell-cell connectivity, a property that ultimately regulates juxtracrine signaling and is pivotal for primordia patterning and cell fate determination (Sharma et al., 2019; Tung et al., 2012). In this context, our study points towards an effect of scutoids on the regulation of the physiological properties of tissues. Therefore, our findings, on top of being fundamental to understand self-organization of epithelia in 3D, open new ways to investigate, and draw implications about, primary developmental processes in which epithelial bending is essential such as tubulogenesis, gastrulation, or neurulation.

Our study also provides important methodological advances. Previous software developed to identify the outlines of the epithelial cells does not work on 3D or lacks enough precision to extract the geometrical and topological data needed to quantify tissue packing in 3D (Bassel et al., 2014; Gómez-Gálvez et al., 2018; Heller et al., 2016; Khan et al., 2014). Here we have shown that our methodological pipeline (**Materials and Methods**) allows to implement a 3D segmentation and the precise reconstruction of cells in epithelia subjected to curvature. We stress that this level of detail is necessary to be able to quantify the apico-basal intercalation phenomenon and, therefore, compare the results with the computational models and extract

bioRxiv preprint doi: https://doi.org/10.1101/2020.02.19.955567; this version posted June 21, 2020. The copyright holder for this preprint (which was not certified by peer review) is the author/funder, who has granted bioRxiv a license to display the preprint in perpetuity. It is made available under aCC-BY-NC-ND 4.0 International license.

biological consequences. We then argue that our methodology, by enabling the analysis of 3D packing in a realistic way, will benefit the field of morphogenesis by bringing understanding about the cellular and mechanical basis of self-organization in curved tissues (Ambrosini et al., 2017; Hirashima and Adachi, 2019; Inoue et al., 2019) or even whole embryos (Shahbazi et al., 2019). In addition, our analysis indicates that the Flintstones' law can be used quantitatively to estimate key connectivity-related parameters, e.g., β and/or $\langle N_{max} \rangle$. This avoids the burden of solving the optimization problem associated with the Kolmogorov model that is computationally demanding (**Material and Methods**). Thus, the values obtained by means of fittings to the Flintstones' law are, at the very least, within the same order of magnitude with respect to the 'exact' Kolmogorov calculations (**Table S1**). This reveals the usability of the Flintstones' law not just as a principle that is satisfied by tubular epithelia, but as a practical way to connect packing properties, geometrical descriptors, and biophysical traits due to its predictive character.

As a matter of discussion, the connectivity law that we have introduced herein, depends on a prediction obtained from the Voronoi computational model that was confirmed in experiments: the "poor get richer" principle. Roughly speaking, we have shown that the fewer neighbors a cell has on a surface, the larger is the probability of a connectivity increase. Interestingly, a similar idea has been reported in T1 dynamical processes during the remodeling of planar epithelia (Bi et al., 2014). Since the scutoidal geometry can be related to planar T1 transitions by exchanging the concepts of space and time, this result reinforces the idea of the existence of universal principles driving the organization of tissues.

In our study we have found that in real tissues the energy cost per 3D neighbor that a cell requires to increase its connectivity, β, is larger than in Voronoi models. We hypothesize that it is due to the purely geometrical description used in the latter. That is, while in *in silico* models the apico-basal transitions develop just a result of a topological constraint (Voronoi tessellation), in the salivary glands, on top of topological constraints, the cells must actively remodel their cytoskeleton to make the transitions possible. That component would explain the larger effective cost of gaining new neighbors in

bioRxiv preprint doi: https://doi.org/10.1101/2020.02.19.955567; this version posted June 21, 2020. The copyright holder for this preprint (which was not certified by peer review) is the author/funder, who has granted bioRxiv a license to display the preprint in perpetuity. It is made available under aCC-BY-NC-ND 4.0 International license.

real tissues. The reduced energetic cost for gaining neighbors in the Voronoi computational approach also explains why *in silico* tubes led to a larger limiting average 3D cellular connectivity, $\langle N_{max} \rangle$, and the V8 model with the same surface ratio that the salivary gland, $s_b = 4$, developed more apico-basal transitions than the real samples (**Fig. 5E**, **Fig. S4**, and **Table S1**). These data ultimately explain why it is necessary to rescale appropriately s_b to obtain a computational model with packing, topological, and connectivity properties similar to those of the salivary glands. In that regard, our results suggest that salivary glands are optimized to reach a high cellular connectivity. While the *in silico* V8 model with a radial expansion of $s_b = 1.75$ or $s_b = 4$ are far for reaching their maximum average connectivity (i.e., $\langle n_{3D} \rangle$'s are, respectively, $\sim 47\%$ and $\sim 61\%$ of $\langle N_{max} \rangle$), in the salivary glands $\langle n_{3D}(s_b) \rangle$ is $\sim 87\%$ of $\langle N_{max} \rangle$ (**Fig. 5E**, **Fig. S4**, and **Table S1**). This optimization could be related to a functionality improvement of the gland, similarly to what has been suggested in pituitary growth hormone secretory cells, where the increase of 3D cellular connectivity has been proposed to better coordinate the pulses of hormone secretion (Bonnefont et al., 2005).

As for the broader implications of our findings, we argue that, while our analyses focus on static tissues from the point of view of tissue architecture, our results can also be relevant to understand active 3D tissue remodeling (e.g., fluidization). Recent studies have revealed that active remodeling involves changes in the material-like properties of tissues that can be connected to an increased activity of neighbor exchanges (Mongera et al., 2018; Tetley et al., 2019). In that regard, here we have shown that the physical basis of 3D self-organization (i.e., 3D cellular packing and connectivity) in tubular epithelia effectively relies on a constant amount of energy, β. Thus, arguably, active 3D tissue remodeling would imply dynamical changes on the value of β that would modify the apico-basal intercalation propensity and therefore the material-like properties: the larger β the more solid-like the tissue would behave. Finally, with respect to the applicability of our results to other areas, we expect that the emerging field of organoids will benefit from our discoveries. A precise quantification of 3D connectivity could then help to understand the lack of reproducibility in organoid production, one of the

bioRxiv preprint doi: https://doi.org/10.1101/2020.02.19.955567; this version posted June 21, 2020. The copyright holder for this preprint (which was not certified by peer review) is the author/funder, who has granted bioRxiv a license to display the preprint in perpetuity. It is made available under aCC-BY-NC-ND 4.0 International license.

biggest challenges of the field (Clevers, 2016; Huch et al., 2017; Schutgens et al., 2019). Also, from a medical point of view, it has been recently shown that tissue curvature affects tumor progression due to the imbalance of tensions in apical and basal surfaces of epithelial tubes (Messal et al., 2019). The Flintstones' law explains how cell energetics affect the 3D packing of these cells and therefore may shed light on the mechanism of tumorigenic morphogenesis in tubular organs.

MATERIALS AND METHODS

Immunohistochemistry and confocal imaging of salivary glands

Flies were grown at 25 °C using standard culture techniques. We dissected the salivary glands from third instar larvae of the wild type *Oregon R* strain. After PBS dissection, the glands were fixed using 4% paraformaldehyde in PBS for 20 min. The samples were washed three times for 10 min with PBT (PBS, 0.3% Triton) and then incubated for 1 hr 45 minutes at room temperature with Cy3-labeled phalloidin (Sigma) to label the cell contours of the epithelial cells. Stained larval salivary glands were mounted using Fluoromount-G (Southern Biotech). We used two pieces of double-sided adhesive tape (one on top of each other) as a spacer (Aldaz et al., 2013), so the salivary glands preserve their shape. Images were taken using a Nikon Eclipse Ti-E laser scanning confocal microscope. The images were captured using a ×20 dry objective and 2.5 µm steps between slices. The image stacks were exported as 1024 × 1024 pixels TIFF files.

3D glands segmentation

To segment the salivary gland stacks of images and reconstruct (semi-automatically) the shape of cells in three dimensions we used the FIJI (Schindelin et al., 2012) plugin LimeSeg (Machado et al., 2019). We inferred cell outlines by using surface elements ("Surfels") obtained by placing single ellipsoidal-like seeds on every cell (see https://imagej.net/LimeSeg for details). Once cell outlines were found (**Fig. 5B**-**C**), we exported them as point clouds (output). We developed a custom-made Matlab code (2018a MathWorks) to postprocess the output of LimeSeg in order to correct errors and obtain perfectly segmented salivary glands. In addition, we manually segmented the

bioRxiv preprint doi: https://doi.org/10.1101/2020.02.19.955567; this version posted June 21, 2020. The copyright holder for this preprint (which was not certified by peer review) is the author/funder, who has granted bioRxiv a license to display the preprint in perpetuity. It is made available under aCC-BY-NC-ND 4.0 International license.

lumen of the glands from the images using Adobe Photoshop CS6 and reconstructed it using a Matlab code. To faithfully represent the gland as a cylinder, we selected a subset of cells: cells that were not ductal, neither located at the tip of the gland. For more information about the processing pipeline: https://osf.io/nd5t6/.

To obtain the cellular neighborhood relations of salivary glands for different values of the radial expansion, we proceeded as follows. We calculated the cell height by estimating the distance between the average voxel positions of the apical surface with respect to the average voxel positions of its basal surface, $d(s_a, s_b)$. Then, to capture a concentric radial section of the gland, we linearly extrapolated the equivalent cell height to the given surface ratio, s:

$$d(s_a, s) = d(s_a, s_b)\ \frac{s}{s_b} \tag{3}$$

where $d(s_a, s)$ is the Euclidean distance between the position of the centroid of the cell at the apical surface, $s_a = 1$, and the position of the centroid at a value $s = R/R_a$ of the radial expansion. Finally, to obtain the gland cylindrical radial section for a given value of the radial expansion, s, we collected all voxels between apical and the upper bound of the calculated distance $d(s_a, s)$. Those cylindrical surfaces of the salivary gland were mapped in the Cartesian plane for analysis using a cylindrical coordinates transformation.

Salivary glands measurements

We quantified the following geometrical and topological descriptors of the segmented salivary glands using a custom-made Matlab code:

- Surface ratio expansion (s): Assuming a cylindrical shape for glands, we estimated s by dividing the area of the basal surface of glands by area of the apical surface.
- Polygonal Class. We estimated the number of sides of each cell using the unrolled images (radial cylindrical sections) projected in the Cartesian plane.

Likewise, we carried out the calculations of the percentage of scutoids and the number of apico-basal transitions.

Voronoi tubular model

bioRxiv preprint doi: https://doi.org/10.1101/2020.02.19.955567; this version posted June 21, 2020. The copyright holder for this preprint (which was not certified by peer review) is the author/funder, who has granted bioRxiv a license to display the preprint in perpetuity. It is made available under aCC-BY-NC-ND 4.0 International license.

Using custom-made Matlab code (R2018a) we generated a Voronoi model that simulates the surface of a cylinder unfolded over the Cartesian plane, see details in Gomez-Galvez et al. ((Gómez-Gálvez et al., 2018), **Material and Methods**). The only difference with the cited methodology, is that in this work the Voronoi diagrams has been constructed by means of the Delaunay triangulation technique. Therefore, we just considered the cells' vertices information (cartesian coordinates and connections) for a much faster computation. For each realization, we used an initial set of 200 randomly located seeds on a rectangular domain of 512 (X axis; transverse axis of cylinder) per 4096 (Y axis; longitudinal axis of cylinder). In total, we implemented 20 different realizations (i.e., tubes). We performed this procedure for 10 different initial Voronoi diagrams (Voronoi 1 (V1, random seeds) to Voronoi 10 (V10, more ordered and homogeneous cells). These diagrams represent the apical (inner) surfaces of computational tubes, and they were obtained by applying N-1 times the Lloyd's algorithm (Lloyd, 1982) to the random seeds, where N is then the resulting Voronoi model. For instance, to compute a V1, we use purely random seeds, while to obtain a V4 diagram, it would be required to apply 3 times the Lloyd's algorithm to random seeds. V8 diagrams provide a polygonal organization in apical surfaces as experimentally observed (Main Text and **Fig. S4**). Subsequent radial sections that define computational tubes with different surface ratios were obtained by implementing a radial projection of the Voronoi seeds. For each apical surface of the tube, we generated 40 expansions by incrementing the surface ratios (s_b) using 0.25 steps: 1 (apical), 1.25, 1.5, … ,10 (maximum basal surface).

As for the 3D reconstruction of cells in Voronoi tubes, each set of seeds that characterizes cells on a given cylindrical section defines a unique 2D Voronoi diagram at every surface and hence the corresponding 2D cellular domains. The set of 2D Voronoi regions that belong to the same radially projected seed from the apical to the basal surface then define each 3D cellular shape. Each of the obtained 3D Voronoi cells was further processed using the Matlab function '*alphaShape'* to transform the set of voxels into a compact, solid, object. This reconstruction pipeline was implemented using Matlab (2018a). Code available at https://osf.io/nd5t6/.

bioRxiv preprint doi: https://doi.org/10.1101/2020.02.19.955567; this version posted June 21, 2020. The copyright holder for this preprint (which was not certified by peer review) is the author/funder, who has granted bioRxiv a license to display the preprint in perpetuity. It is made available under aCC-BY-NC-ND 4.0 International license.

Voronoi tubular model measurements.

We measured the following properties of cells in Voronoi tubular models: number of sides of cells for a given radial section, and total number neighbors. Additionally, we computed the percentage of scutoids, the number of apico-basal transitions, the polygon distribution of every surface (radial sections). In these quantifications, we disregarded cells at the boundaries (tips of tubes) to avoid 'border effects'.

In Voronoi tubes the net gain of 3D neighbors is bounded

Assuming a cylindrical geometry (e.g., epithelial tubes), each point at a given radial surface can be represented into the Cartesian plane; where coordinate x accounts for the cylindrical transversal coordinate and coordinate y for the longitudinal one (see **Box**). Thus, if the coordinates of a point (e.g., a Voronoi seed) at the apical surface are given by (x, y), the coordinates of that point at a surface with a value of the cylindrical radial expansion $s \in [1, \infty)$ can be found by defining the function $f_s\colon \mathbb{R}^2 \longrightarrow \mathbb{R}^2$ $f_s(x, y) = (sx, y)$. Under these conditions, we aim to characterize the seeds that generate scutoids (exchanges in the neighboring relations of seeds) as s changes.

Lemma 1. Given three non–colinear points $\{A, B, C\}$ that define a circle (a nearest-neighbors relation), and another exterior point D, if $s > 1$ exists such that $f_s(D)$ is interior to the circle defined by $\{f_s(A), f_s(B), f_s(C)\}$, then D is inside of the vertical parabola containing $\{A, B, C\}$ (**Box**).

Remark. If two of the three points $\{A, B, C\}$ are on the same vertical line, then the parabola considered in Lemma 1 degenerates as a vertical strip. Even in this case, the thesis of the Lemma is true if we replace the interior of the parabola by the inside of the strip.

Proof. Without loss of generality, we can suppose that $\{A, B, C\}$ are counterclockwise oriented and that they have Cartesian coordinates (a_1, a_2), (b_1, b_2) and (c_1, c_2) respectively.

Thus, the point $D(x, y)$ is outside the circle defined by $\{A, B, C\}$ if, and only if, the sign of the following determinant is negative:

bioRxiv preprint doi: https://doi.org/10.1101/2020.02.19.955567; this version posted June 21, 2020. The copyright holder for this preprint (which was not certified by peer review) is the author/funder, who has granted bioRxiv a license to display the preprint in perpetuity. It is made available under aCC-BY-NC-ND 4.0 International license.

$$\begin{vmatrix} a_1 & a_2 & a_1^2+a_2^2 & 1 \\ b_1 & b_2 & b_1^2+b_2^2 & 1 \\ c_1 & c_2 & c_1^2+c_2^2 & 1 \\ x & y & x^2+y^2 & 1 \end{vmatrix} = \begin{vmatrix} a_1 & a_2 & a_1^2 & 1 \\ b_1 & b_2 & b_1^2 & 1 \\ c_1 & c_2 & c_1^2 & 1 \\ x & y & x^2 & 1 \end{vmatrix} + \begin{vmatrix} a_1 & a_2 & a_2^2 & 1 \\ b_1 & b_2 & b_2^2 & 1 \\ c_1 & c_2 & c_2^2 & 1 \\ x & y & y^2 & 1 \end{vmatrix} < 0 \tag{4}$$

For the sake of simplicity, we represent the previous equation as:

$$det(\mathcal{A}) = det(\mathcal{B}) + det(\mathcal{C}) < 0 \tag{5}$$

On the other hand, by considering x and y as variables, the equation $det(\mathcal{A}) = 0$ corresponds to the circle defined by $\{A, B, C\}$, and $det(\mathcal{B}) = 0$ corresponds to the vertical parabola defined by the same three points. Consequently, the inequality $det(\mathcal{B}) > 0$ defines the locus of interior points to that parabola.

Now, assuming that $s > 1$ exists such that $f_s(D)$ is interior to the circle defined by $\{f_s(A), f_s(B), f_s(C)\}$. Then,

$$\begin{vmatrix} sa_1 & a_2 & s^2a_1^2+a_2^2 & 1 \\ sb_1 & b_2 & s^2b_1^2+b_2^2 & 1 \\ sc_1 & c_2 & s^2c_1^2+c_2^2 & 1 \\ sx & y & s^2x^2+y^2 & 1 \end{vmatrix} = s^3\, det(\mathcal{B}) + s\, det(\mathcal{C}) > 0 \tag{6}$$

Or, equivalently, $s^2\, det(\mathcal{B}) + det(\mathcal{C}) > 0$, so, $s^2\, det(\mathcal{B}) > -det(\mathcal{C})$. If $det(\mathcal{B}) < 0$, then $1 < s^2 < -\frac{det(\mathcal{C})}{det(\mathcal{B})}$ and therefore $det(\mathcal{B}) > -det(\mathcal{C})$. The latter is in contradiction with $det(\mathcal{B}) + det(\mathcal{C}) < 0$. As a result, $det(\mathcal{B}) > 0$, and the following inequality holds,

$$s^2 > -\frac{det(\mathcal{C})}{det(\mathcal{B})} > 1 \tag{7}$$

Notice that if the circle defined by $\{A, B, C\}$ is surrounded by a set of points and we change continuously the parameter s in the interval $[1, \infty)$, it is possible to detect the first point touching the circle defined by $\{f_s(A), f_s(B), f_s(C)\}$. That point can be obtained by computing all the points at $s = \sqrt{-\frac{det(\mathcal{C})}{det(\mathcal{B})}}$. Hence, the first point contacting the circle will be that with the minimum value of s.

bioRxiv preprint doi: https://doi.org/10.1101/2020.02.19.955567; this version posted June 21, 2020. The copyright holder for this preprint (which was not certified by peer review) is the author/funder, who has granted bioRxiv a license to display the preprint in perpetuity. It is made available under aCC-BY-NC-ND 4.0 International license.

As for proving that the average of the number of neighbours of a cell induced by a seed grows is bounded as a function of the surface ratio, we state the following proposition:

Proposition 1. Given a Voronoi seed representing a cell, if $n_{3D}(s)$ is the total number of accumulated cell neighbors as s increases from $s = 1$ (apical surface) to a given value of s, then $\langle n_{3D}(s)\rangle$ is a bounded function for a finite cylinder.

Proof. We model the apical surface as the cylinder $2\pi r \times h$, where r representes the inner radius and h the length of the cylinder. Given a seed A in that surface, in the corresponding Delaunay triangulation it appears as a point surrounded by triangles defining the neighbourhood of A. By Lemma 1, each triangle defines a vertical parabola and a circle. So, any other seed touching A in other layer must be inside of one of the parabolas and outside of all circles (see **Box**). Let's denote $\mathcal{R}_{s,A}$ the feasible region for a new neighbour of A in the layer represented by s, i.e., all points inside one of the parabolas and outside all the circles. Thus, if $\#(\mathcal{R}_{s,A})$ is the number of seeds in that region that are not neighbours of A in the apical surface, obviously, an upper bound to the number of new neighbours to A is given by $\#(\mathcal{R}_{s,A}) \leq \#(\mathcal{R}_{1,A})$.

On the other hand, that number of seeds is, in average, proportional to the density of seeds times the area of $\mathcal{R}_{s,A}$, therefore, the average number of accumulated neighbours of A, denoted as $\langle n_{3D}(A)\rangle$, will be bounded by the change of the density of points when growing s, this is to say,

$$d\langle n_{3D}(A)\rangle \leq M \cdot \frac{\mathcal{R}_{s,A}}{2\pi s r \cdot h}\, ds \tag{8}$$

where M represents the total number of seeds (i.e., the total number of cells that is a constant) and the quotient is the area of $\mathcal{R}_{s,A}$ divided by the area of a given radial layer. In general, it is not possible to integrate equation (4), since the area of $\mathcal{R}_{s,A}$ is known only in very few, particular, cases.

bioRxiv preprint doi: https://doi.org/10.1101/2020.02.19.955567; this version posted June 21, 2020. The copyright holder for this preprint (which was not certified by peer review) is the author/funder, who has granted bioRxiv a license to display the preprint in perpetuity. It is made available under aCC-BY-NC-ND 4.0 International license.

If the case of a finite cylinder, $\langle n_{3D}(A)\rangle \leq \#(\mathcal{R}_{s,A}) \leq \#(\mathcal{R}_{1,A})$ leads, suming up to all the seeds and dividing by M, to the upper bound

$$\langle n_{3D}(s)\rangle \leq \frac{1}{M} \cdot \sum_A \#(\mathcal{R}_{1,A}) \quad (9)$$

thus, $\langle n_{3D}(s)\rangle$ is necessarily a bounded function. This expression indicates that the number of new neighbours when increasing s exhausts since the number of cells is a resource shared by all the layers. It is possible to obtain an upper bound to $\langle N_{max}\rangle = \lim_{s\to\infty}\langle n_{3D}(s)\rangle$ since, after a flip in the Delaunay triangulation, the edge disappearing (i.e., a cell contact loss) can never be recovered in a cylindrical geometry. Thus, $M \cdot \left(\langle N_{max}\rangle - n_{3D}(1)\right)$ is bounded by the number of edges that complement the original Delaunay triangulation on the apical surface, that is,

$$\langle N_{max}\rangle - \langle n_{3D}(1)\rangle \leq \frac{1}{M} \cdot \left(\frac{M(M-1)}{2} - M\frac{\langle n_{3D}(1)\rangle}{2}\right) = \frac{M-1}{2} - \frac{\langle n_{3D}(1)\rangle}{2} \quad (10)$$

leading to

$$\langle N_{max}\rangle \leq \frac{M-1}{2} + \frac{\langle n_{3D}(1)\rangle}{2} \leq \frac{M-1}{2} + 3 = \frac{M+5}{2} \quad (11)$$

Where we have assumed that $\langle n_{3D}(1)\rangle = 6$. The simulations of the computational Voronoi model and the data of the salivary gland show that $\langle N_{max}\rangle$ is in fact much smaller that the theoretical bound $\frac{M+5}{2}$.

Relation between total accumulated 3D neighbors and the number of intercalation events

Scutoids have a Euler characteristic $\chi = 2$ such that $V - E + F = 2$, where V, E, and F accounts for the number of vertexes, edges, and faces respectively. We assumed that the apical, a, and basal, b, faces of scutoids tesellating a cylindrical space have radial coordinates R_a and R_b respectively. Then, for any value of the surface ratio expansion, $s = R/R_a$, these solids can be mapped into a connected plane graph with the same Euler characteristic (a sort of projection of the vertexes and connectors into the plane, see **Fig. S5.** Thus, as a function of s, the accumulated number of 3D neighbors reads $n_{3D}(s) = E(s) - V(s)$. Since in tubular geometries the radially projected seeds from the

bioRxiv preprint doi: https://doi.org/10.1101/2020.02.19.955567; this version posted June 21, 2020. The copyright holder for this preprint (which was not certified by peer review) is the author/funder, who has granted bioRxiv a license to display the preprint in perpetuity. It is made available under aCC-BY-NC-ND 4.0 International license.

apical to the basal surface never come closer, as s increases (i.e., apico-basal intercalations are not reversible).

$$n_{3D}(s) = max(\{V(s)\}) = min(\{V(s)\}) + i(s) \tag{12}$$

where $\{V(s)\} = \{V(1), V(1+ds), \cdots, V(s_b)\}$ and $i(s)$ denotes the number of intercalation points in the interval $s \in [1, s_b]$. In the case of a 3D tessellation with N cells, where M of them do not show any intercalation, the total number of accumulated neighbors reads,

$$n_{3D}(s) = \sum_{j=1}^{N} n_{3D}^{(j)}(s) = \sum_{j=1}^{M} V^{(j)}(1) + \sum_{j=1}^{N-M} max\left(\left\{V^{(j)}(s)\right\}\right) = \sum_{j=1}^{M} V^{(j)}(1) + \sum_{j=1}^{N-M}\left\{min\left(\left\{V^{(j)}(s)\right\}\right) + i^{(j)}(s)\right\} \tag{13}$$

Given that each intercalation point is shared by four cells, two of them necessarily increase their number of vertices in a given s-plane and two of them decrease their number of vertices (see **Fig. 1A**). Thus, in the case of a decrease $max\left(\left\{V^{(j)}(s)\right\}\right) = V^{(j)}(1)$ and in the case of an increase $min\left(\left\{V^{(j)}(s)\right\}\right) + i^{(j)}(s) = V^{(j)}(1) + i^{(j)}(s)$. Consequently,

$$n_{3D}(s) = \sum_{j=1}^{N} V^{(j)}(1) + \sum_{j=1}^{(N-M)/2} i^{(j)}(s) = \sum_{j=1}^{N} V^{(j)}(1) + \frac{1}{2}\sum_{j=1}^{N-M} i^{(j)}(s) \tag{14}$$

where we used the fact that for every intercalation event that increases by one the number of neighbors there is one that decreases the number of neighbors in the same amount; consequently, we can add up all intercalation events and divide by two. Hence the average number of accumulated 3D neighbors, $\langle n_{3D}(s)\rangle = n_{3D}(s)/N$ reads $\langle n_{3D}(s)\rangle = \langle V(1)\rangle + \langle i(s)\rangle/2$; $\langle i(s)\rangle$ being the average number of apico-basal intercalations per cell. Finally, by considering that any s-surface, and in particular the apical surface $s = 1$, corresponds to a 2D tessellation of convex polygons, $\langle V(1)\rangle = 6$ we conclude that,

$$\langle n_{3D}(s)\rangle = 6 + \frac{1}{2}\langle i(s)\rangle \tag{15}$$

A Kolmogorov rate equation for the 3D cellular connectivity

bioRxiv preprint doi: https://doi.org/10.1101/2020.02.19.955567; this version posted June 21, 2020. The copyright holder for this preprint (which was not certified by peer review) is the author/funder, who has granted bioRxiv a license to display the preprint in perpetuity. It is made available under aCC-BY-NC-ND 4.0 International license.

The probability, P, of having m accumulated 3D neighbors (i.e., $m = n_{3D}$) as the surface ratio increases from s to $s + ds$ can be described by the following Markov equation (**Fig. 4B**),

$$P_m(s + ds) = P_m(s)T_{m,m} + P_{m-1}(s)T_{m-1,m} \tag{16}$$

where $T_{i,j}$ is the probability of incrementing the number of neighbors from i to j due to an apico-basal intercalation. Since $\sum_j T_{i,j} = 1$ (normalization of the transition probabilities) and $T_{i,j} = f(i,j)\{\delta_{i-1,j} + \delta_{i,j+1}\}$ (each intercalation can only possibly induce to win one neighbor) then $T_{m,m} = 1 - T_{m,m+1}$ and the above Markov equation can be written as a Kolmogorov equation (a.k.a. Master equation):

$$\frac{dP_m(s)}{ds} = P_{m-1}(s)r_{m-1,m} - P_m(s)r_{m,m+1} \tag{17}$$

where $r_{i,j}$ accounts for the probability of apico-basal intercalations per unit of surface ratio, i.e., $T_{i,j} = r_{i,j}ds$.

If we assume an Arrhenius-like kinetics (i.e., in order to win an additional neighbor there is an energy cost, see (Bi et al., 2014)) then $r_{i,i+1} = \hat{\alpha}e^{-\Delta E_i}$, where $\hat{\alpha}$ is the so-called pre-exponential factor that modulates the "bare" frequency of intercalations (per unit of surface ratio expansion) and ΔE_i is the activation energy in some energy units. In our case in units of E_0: the value of the energetic barrier of the four-fold vertex configuration (**Fig. 4A**). The observed "poor get richer" behavior suggests that the activation energy, ΔE_i, increases with i. For the sake of simplicity, up to first order in i: $\Delta E_i = i \cdot \beta$ (β being the dimensionless activation energy of a cell per 3D neighbor in units of E_0). On the other hand, the mathematical calculations (see Eq. (9)) indicate that the intercalation rate $r_{i,i+1}$ becomes null for a finite value of i or, alternatively, that the activation energy becomes infinite for a finite value of i. Otherwise, the net gain of new neighbors is not bounded. This fact can be accounted for by assuming that the bare frequency is a function of the number of neighbors, $\hat{\alpha} = \hat{\alpha}(i)$, such that $\frac{d\hat{\alpha}}{di} < 0$ and becomes null for a finite value of i. Again, for the sake of simplicity, we assume that up to first order in i: $\hat{\alpha} = \alpha(N_{max} - i)$, where N_{max} is the asymptotic, maximum, number of 3D

bioRxiv preprint doi: https://doi.org/10.1101/2020.02.19.955567; this version posted June 21, 2020. The copyright holder for this preprint (which was not certified by peer review) is the author/funder, who has granted bioRxiv a license to display the preprint in perpetuity. It is made available under aCC-BY-NC-ND 4.0 International license.

neighbors a cell can possibly have. Summarizing, we assume that the apico-basal intercalation rate $r_{i,i+1}$ reads,

$$r_{i,i+1} = \alpha(N_{max} - i)e^{-i\beta} \quad (18)$$

Under these conditions, the Kolmogorov equation reads,

$$\frac{dP_m(s)}{ds} = \alpha\big(N_{max} - (m-1)\big)e^{-\beta(m-1)}P_{m-1}(s) - \alpha(N_{max} - m)e^{-\beta m}P_m(s) \quad (19)$$

On the other hand, the equation satisfied by the average number of accumulated 3D neighbors, $\langle n_{3D}\rangle = \langle m\rangle$, reads,

$$\frac{d\langle m(s)\rangle}{ds} = \sum_m m\frac{dP_m(s)}{ds} = \sum_m r_{m,m+1}P_m(s) = \langle r_{m,m+1}\rangle \quad (20)$$

Alternatively, in order to obtain an analytical expression able to recapitulate, effectively, the mathematical principle that govern the net gain of 3D neighbors, we perform the following approximations. First, we perform a mean-field-like approximation, i.e., $\langle F(m)\rangle \approx F(\langle m\rangle)$,

$$\frac{d\langle m\rangle}{ds} \approx \alpha(\langle N_{max}\rangle - \langle m\rangle)e^{-\beta\langle m\rangle} \quad (21)$$

Where $\langle N_{max}\rangle$ is the limiting average cellular connectivity. Second, since $\beta < 1$,

$$\frac{d\langle m\rangle}{ds} \approx \alpha(\langle N_{max}\rangle - \langle m\rangle)(1 - \beta\langle m\rangle) + \mathcal{O}(\beta^2) \quad (22)$$

Equation (21) is formally a logistic-like growth equation,

$$\frac{d\langle m\rangle}{ds} = \frac{b}{c(b-d)}(\langle N_{max}\rangle - \langle m\rangle)\left(1 - \frac{d}{bN_{max}}\langle m\rangle\right) \quad (23)$$

that has as solution,

$$\langle m(s)\rangle = \langle N_{max}\rangle\frac{1+be^{-\frac{s}{c}}}{1+de^{-\frac{s}{c}}} \quad (24)$$

Thus, if $c > 0$ then $\lim_{s\to\infty}\langle m(s)\rangle = \langle N_{max}\rangle$. The parameters b, c, and d are further constrained by the following facts: $\frac{d\langle m\rangle}{ds} > 0$ (3D neighbors can only accumulate) and $\frac{d^2\langle m\rangle}{ds^2} < 0$ ("poor get richer" principle). Moreover, if we impose the condition $\langle m(1)\rangle = 6$ (the average number of neighbors in the apical surface is 6) these parameters are not independent since,

bioRxiv preprint doi: https://doi.org/10.1101/2020.02.19.955567; this version posted June 21, 2020. The copyright holder for this preprint (which was not certified by peer review) is the author/funder, who has granted bioRxiv a license to display the preprint in perpetuity. It is made available under aCC-BY-NC-ND 4.0 International license.

$$b = \frac{6d - (\langle N_{max} \rangle - 6) e^{\frac{1}{c}}}{\langle N_{max} \rangle} \tag{25}$$

All the above implies that the logistic-like fitting function, Eq. (24), describes, approximately but effectively, the analytical mathematical law ("Flintstone's law") underlying the 3D average connectivity if the following conditions hold, either $-1 < d < 0$ or $c \ln(-d) < 1$ if $d < -1$.

The relation between the fitting parameters of the logistic fitting with α and β are,

$$\alpha = \frac{b}{c(b-d)} \tag{26}$$

$$\beta = \frac{d}{b\langle N_{max} \rangle} \tag{27}$$

For finding the parameters α and β in *in silico* tubes and salivary glands we then implemented two possible approaches. On the one hand, we implemented an error minimization algorithm that recursively solved, numerically, Eq. (20) to obtain $\langle m(s) \rangle = \sum_m m P_m(s)$ taking also into account the normalization condition $\sum_{m=1}^{\infty} P_m(s) = 1$ (code available at https://osf.io/nd5t6).

On the other hand, we obtained values using the fitting logistic function Eq. (24). We notice that the values obtained through the first method are exact as compared to the values obtained from the fitting that are based on a series of approximations as explained above (see **Table S1**).

The values of α and β are obtained from the exact methodology were further used to compare the predicted probability distribution of having m accumulated neighbors for a given value of s: $P_m(s)$. We evaluated the relative error of this prediction with respect to the actual distribution from data, $P_m^{actual}(s)$, by computing $\varepsilon^2 = \frac{1}{2}\sum_m \left(P_m^{actual}(s) - P_m(s)\right)^2$. This quantity is normalized such that in case of the following situation of full disagreement between the distributions, $P_m^{actual}(s) = \delta_{m,i}$ and $P_m(s) = \delta_{m,j}$ with $i \neq j$, provides $\varepsilon^2 = 1$ (i.e., 100% error).

Quantitative characterization of spreading in neighbor exchange distributions between apical and basal surfaces

bioRxiv preprint doi: https://doi.org/10.1101/2020.02.19.955567; this version posted June 21, 2020. The copyright holder for this preprint (which was not certified by peer review) is the author/funder, who has granted bioRxiv a license to display the preprint in perpetuity. It is made available under aCC-BY-NC-ND 4.0 International license.

In order to characterize the spreading away from the diagonal in the neighbor exchange distributions between apical and basal surfaces, **Fig. 2A-B**, we followed the same approach used to quantify intrinsic noise during gene expression processes (see (Elowitz, 2002). Thus, $\eta^2 = \frac{\langle (n_a - n_b)^2 \rangle}{2\langle n_a \rangle \langle n_b \rangle}$ where $\langle z(n_a, n_b) \rangle = \sum_{n_a, n_b} z(n_a, n_b) p(n_a, n_b)$; z representing any function of n_a and n_b and $p(n_a, n_b)$ being the probability of neighbor exchange events.

Logistic data fitting

To obtain the logistic function that fit best our data points, we analyzed all the possible parameters combination and achieved the global minimum solution. This 'fit' was based on the 'least squares' method and minimizes the residual $r = \sum_{i=1}^{n} (y_i - y_i')^2$ where, y_i and y_i' stand for the observed values and the fitted ones, respectively. The logistic equation (Eq. (24)):

$$f(s) = \langle N_{max} \rangle \frac{1 + b e^{-\frac{s}{c}}}{1 + d e^{-\frac{s}{c}}} \tag{28}$$

was then fitted to find the average 3D cell connectivity, but with a series of constraints on the parameters (as explained above): $\langle f(s = 1) \rangle = 6$, $c > 0$, $d < 0$, $\langle N_{max} \rangle \geq 0$, $d > b$ and if $d < -1$ then $c \ln(-d) < 1$. The goodness of fitting was estimated by means of the coefficient of determination, R^2.

Data availability

All the necessary material to reproduce this study is available at the Center for Open Science repository: https://osf.io/nd5t6.

bioRxiv preprint doi: https://doi.org/10.1101/2020.02.19.955567; this version posted June 21, 2020. The copyright holder for this preprint (which was not certified by peer review) is the author/funder, who has granted bioRxiv a license to display the preprint in perpetuity. It is made available under aCC-BY-NC-ND 4.0 International license.

REFERENCES

Aldaz, S., Escudero, L.M., and Freeman, M. (2013). Dual role of myosin II during Drosophila imaginal disc metamorphosis. Nat. Commun. *4*, 1761.

Alt, S., Ganguly, P., and Salbreux, G. (2017). Vertex models: from cell mechanics to tissue morphogenesis. Philos. Trans. R. Soc. B Biol. Sci. *372*, 20150520.

Ambrosini, A., Gracia, M., Proag, A., Rayer, M., Monier, B., and Suzanne, M. (2017). Apoptotic forces in tissue morphogenesis. Mech. Dev. *144*, 33–42.

Arganda-Carreras, I., Kaynig, V., Rueden, C., Eliceiri, K.W., Schindelin, J., Cardona, A., and Sebastian Seung, H. (2017). Trainable Weka Segmentation: a machine learning tool for microscopy pixel classification. Bioinformatics *33*, 2424–2426.

Bassel, G.W., Stamm, P., Mosca, G., Barbier de Reuille, P., Gibbs, D.J., Winter, R., Janka, A., Holdsworth, M.J., and Smith, R.S. (2014). Mechanical constraints imposed by 3D cellular geometry and arrangement modulate growth patterns in the Arabidopsis embryo. Proc. Natl. Acad. Sci. *111*, 8685–8690.

Bertet, C., Sulak, L., and Lecuit, T. (2004). Myosin-dependent junction remodelling controls planar cell intercalation and axis elongation. Nature *429*, 667–671.

Bi, D., Lopez, J.H., Schwarz, J.M., and Lisa Manning, M. (2014). Energy barriers and cell migration in densely packed tissues. Soft Matter *10*, 1885–1890.

Bi, D., Lopez, J.H., Schwarz, J.M., and Manning, M.L. (2015). A density-independent rigidity transition in biological tissues. Nat. Phys. *11*, 1074–1079.

Bonnefont, X., Lacampagne, A., Sanchez-Hormigo, A., Fino, E., Creff, A., Mathieu, M.-N., Smallwood, S., Carmignac, D., Fontanaud, P., Travo, P., et al. (2005). Revealing the large-scale network organization of growth hormone-secreting cells. Proc. Natl. Acad. Sci. *102*, 16880–16885.

Box, K., Joyce, B.W., and Devenport, D. (2019). Epithelial geometry regulates spindle orientation and progenitor fate during formation of the mammalian epidermis. Elife *8*, e47102.

Campàs, O., Mammoto, T., Hasso, S., Sperling, R.A., O'Connell, D., Bischof, A.G., Maas, R., Weitz, D.A., Mahadevan, L., and Ingber, D.E. (2014). Quantifying cell-generated mechanical forces within living embryonic tissues. Nat. Methods *11*, 183–189.

Canela-Xandri, O., Sagués, F., Casademunt, J., and Buceta, J. (2011). Dynamics and Mechanical Stability of the Developing Dorsoventral Organizer of the Wing Imaginal Disc. PLoS Comput. Biol. *7*, e1002153.

Clevers, H. (2016). Modeling Development and Disease with Organoids. Cell *165*, 1586–1597.

Colas, J.-F., and Schoenwolf, G.C. (2001). Towards a cellular and molecular understanding of neurulation. Dev. Dyn. *221*, 117–145.

Curran, S., Strandkvist, C., Bathmann, J., de Gennes, M., Kabla, A., Salbreux, G., and Baum, B. (2017). Myosin II Controls Junction Fluctuations to Guide Epithelial Tissue Ordering. Dev. Cell *43*, 480-492.e6.

bioRxiv preprint doi: https://doi.org/10.1101/2020.02.19.955567; this version posted June 21, 2020. The copyright holder for this preprint (which was not certified by peer review) is the author/funder, who has granted bioRxiv a license to display the preprint in perpetuity. It is made available under aCC-BY-NC-ND 4.0 International license.

Elowitz, M.B. (2002). Stochastic Gene Expression in a Single Cell. Science (80-.). *297*, 1183–1186.

Farhadifar, R., Röper, J.-C., Aigouy, B., Eaton, S., and Jülicher, F. (2007). The Influence of Cell Mechanics, Cell-Cell Interactions, and Proliferation on Epithelial Packing. Curr. Biol. *17*, 2095–2104.

Fletcher, A.G., Osterfield, M., Baker, R.E., and Shvartsman, S.Y. (2014). Vertex models of epithelial morphogenesis. Biophys. J. *106*, 2291–2304.

Gibson, M.C., Patel, A.B., Nagpal, R., and Perrimon, N. (2006). The emergence of geometric order in proliferating metazoan epithelia. Nature *442*, 1038–1041.

Gibson, W.T., Veldhuis, J.H., Rubinstein, B., Cartwright, H.N., Perrimon, N., Brodland, G.W., Nagpal, R., and Gibson, M.C. (2011). Control of the mitotic cleavage plane by local epithelial topology. Cell *144*, 427–438.

Gilbert, S.F., and Barresi, M.J.F. (2016). Developmental biology (Sunderland, MA Sinauer Associates).

Girdler, G.C., and Röper, K. (2014). Controlling cell shape changes during salivary gland tube formation in Drosophila. Semin. Cell Dev. Biol. *31*, 74–81.

Gómez-Gálvez, P., Vicente-Munuera, P., Tagua, A., Forja, C., Castro, A.M.A.M., Letrán, M., Valencia-Expósito, A., Grima, C., Bermúdez-Gallardo, M., Serrano-Pérez-Higueras, Ó., et al. (2018). Scutoids are a geometrical solution to three-dimensional packing of epithelia. Nat. Commun. *9*, 2960.

Heller, D., Hoppe, A., Restrepo, S., Gatti, L., Tournier, A.L.L., Tapon, N., Basler, K., and Mao, Y. (2016). EpiTools: An Open-Source Image Analysis Toolkit for Quantifying Epithelial Growth Dynamics. *36*, 103–116.

Hirashima, T., and Adachi, T. (2019). Polarized cellular mechano-response system for maintaining radial size in developing epithelial tubes. Development *146*, dev181206.

Honda, H. (1978). Description of cellular patterns by Dirichlet domains: the two-dimensional case. J Theor Biol *72*, 523–543.

Huch, M., Knoblich, J.A., Lutolf, M.P., and Martinez-Arias, A. (2017). The hope and the hype of organoid research. Dev. *144*, 938–941.

Huebner, R.J., and Ewald, A.J. (2014). Cellular foundations of mammary tubulogenesis. Semin. Cell Dev. Biol. *31*, 124–131.

Inoue, Y., Tateo, I., and Adachi, T. (2019). Epithelial tissue folding pattern in confined geometry. Biomech. Model. Mechanobiol.

Iruela-Arispe, M.L., and Beitel, G.J. (2013). Tubulogenesis. Development *140*, 2851–2855.

Irvine, K.D., and Wieschaus, E. (1994). Cell intercalation suring Drosophila germband extension and its regulaton by pair00rule segmentation genes. Development *120*, 827–841.

Khan, Z., Wang, Y.-C., Wieschaus, E.F., and Kaschube, M. (2014). Quantitative 4D analyses of epithelial folding during Drosophila gastrulation. Development *141*, 2895–2900.

Latorre, E., Kale, S., Casares, L., Gómez-González, M., Uroz, M., Valon, L., Nair, R. V., Garreta, E., Montserrat, N., del Campo, A., et al. (2018). Active superelasticity in three-dimensional epithelia of controlled shape. Nature *563*, 203–208.

bioRxiv preprint doi: https://doi.org/10.1101/2020.02.19.955567; this version posted June 21, 2020. The copyright holder for this preprint (which was not certified by peer review) is the author/funder, who has granted bioRxiv a license to display the preprint in perpetuity. It is made available under aCC-BY-NC-ND 4.0 International license.

Leptin, M., and Grunewald, B. (1990). Cell shape changes during gastrulation in Drosophila. Development *110*, 73–84.

Lewis, F.T. (1928). The correlation between cell division and the shapes and sizes of prismatic cells in the epidermis of cucumis. Anatom. Rec. *38*, 341–376.

Lloyd, S. (1982). Least squares quantization in PCM. IEEE Trans. Inf. Theory *28*, 129–137.

Machado, S., Mercier, V., and Chiaruttini, N. (2019). LimeSeg: a coarse-grained lipid membrane simulation for 3D image segmentation. BMC Bioinformatics *20*, 2.

Mao, Y., Tournier, A.L., Hoppe, A., Kester, L., Thompson, B.J., and Tapon, N. (2013). Differential proliferation rates generate patterns of mechanical tension that orient tissue growth. EMBO J. *32*, 2790–2803.

Messal, H.A., Alt, S., Ferreira, R.M.M., Gribben, C., Wang, V.M.-Y., Cotoi, C.G., Salbreux, G., and Behrens, A. (2019). Tissue curvature and apicobasal mechanical tension imbalance instruct cancer morphogenesis. Nature *566*, 126.

Misra, M., Audoly, B., and Shvartsman, S.Y. (2017). Complex structures from patterned cell sheets. Philos. Trans. R. Soc. B Biol. Sci. *372*, 20150515.

Mongera, A., Rowghanian, P., Gustafson, H.J., Shelton, E., Kealhofer, D.A., Carn, E.K., Serwane, F., Lucio, A.A., Giammona, J., and Campàs, O. (2018). A fluid-to-solid jamming transition underlies vertebrate body axis elongation. Nature *561*, 401–405.

Mughal, A., Cox, S.J., Weaire, D., Burke, S.R., and Hutzler, S. (2018). Demonstration and interpretation of 'scutoid' cells formed in a quasi-2D soap froth. Philos. Mag. Lett. *98*, 358–364.

Nelson, C.M. (2009). Geometric control of tissue morphogenesis. Biochim. Biophys. Acta - Mol. Cell Res. *1793*, 903–910.

Nelson, C.M., Jean, R.P., Tan, J.L., Liu, W.F., Sniadecki, N.J., Spector, A.A., and Chen, C.S. (2005). Emergent patterns of growth controlled by multicellular form and mechanics. Proc. Natl. Acad. Sci. *102*, 11594–11599.

Okuda, S., Kuranaga, E., and Sato, K. (2019). Apical Junctional Fluctuations Lead to Cell Flow while Maintaining Epithelial Integrity. Biophys. J. *116*, 1159–1170.

Pérez-González, C., Alert, R., Blanch-Mercader, C., Gómez-González, M., Kolodziej, T., Bazellieres, E., Casademunt, J., and Trepat, X. (2019). Active wetting of epithelial tissues. Nat. Phys. *15*, 79–88.

Pilot, F., and Lecuit, T. (2005). Compartmentalized morphogenesis in epithelia: from cell to tissue shape. Dev Dyn *232*, 685–694.

Reinhardt, K. (1918). Über die Zerlegung der Ebene in Polygone.

Röper, K. (2018). Quantitative Imaging and the Effect of Tissue Topology on Morphogenesis. Dev. Cell *47*, 537–538.

Rupprecht, J.F., Ong, K.H., Yin, J., Huang, A., Dinh, H.H.Q., Singh, A.P., Zhang, S., Yu, W., and Saunders, T.E. (2017). Geometric constraints alter cell arrangements within curved epithelial tissues. Mol. Biol. Cell *28*, 3582–3594.

Sanchez-Corrales, Y.E., Blanchard, G.B., and Röper, K. (2018). Radially patterned cell behaviours during tube budding from an epithelium. Elife *7*,

bioRxiv preprint doi: https://doi.org/10.1101/2020.02.19.955567; this version posted June 21, 2020. The copyright holder for this preprint (which was not certified by peer review) is the author/funder, who has granted bioRxiv a license to display the preprint in perpetuity. It is made available under aCC-BY-NC-ND 4.0 International license.

e35717.

Sánchez-Gutiérrez, D., Tozluoglu, M., Barry, J.D., Pascual, A., Mao, Y., and Escudero, L.M. (2016). Fundamental physical cellular constraints drive self-organization of tissues. EMBO J. *35*, 77–88.

Schindelin, J., Arganda-Carreras, I., Frise, E., Kaynig, V., Longair, M., Pietzsch, T., Preibisch, S., Rueden, C., Saalfeld, S., Schmid, B., et al. (2012). Fiji: an open-source platform for biological-image analysis. Nat. Methods *9*, 676–682.

Schutgens, F., Rookmaaker, M.B., Margaritis, T., Rios, A., Ammerlaan, C., Jansen, J., Gijzen, L., Vormann, M., Vonk, A., Viveen, M., et al. (2019). Tubuloids derived from human adult kidney and urine for personalized disease modeling. Nat. Biotechnol. *37*, 303–313.

Shahbazi, M.N., Siggia, E.D., and Zernicka-Goetz, M. (2019). Self-organization of stem cells into embryos: A window on early mammalian development. Science (80-.). *364*, 948–951.

Sharma, P., Saraswathy, V.M., Xiang, L., and Furthauer, M. (2019). Delta/Notch signaling controls neuroepithelial morphogenesis in the zebrafish spinal cord. BioRxiv 517714.

Siedlik, M.J., Manivannan, S., Kevrekidis, I.G., and Nelson, C.M. (2017). Cell Division Induces and Switches Coherent Angular Motion within Bounded Cellular Collectives. Biophys. J. *112*, 2419–2427.

Spencer, M.A., Jabeen, Z., and Lubensky, D.K. (2017). Vertex stability and topological transitions in vertex models of foams and epithelia. Eur. Phys. J. E *40*, 2.

Sugimura, K., Lenne, P.-F.F., and Graner, F. (2016). Measuring forces and stresses in situ in living tissues. Development *143*, 186–196.

Swanson, L.E., and Beitel, G.J. (2006). Tubulogenesis: an inside job. Curr Biol *16*, R51-3.

Tetley, R.J., Staddon, M.F., Heller, D., Hoppe, A., Banerjee, S., and Mao, Y. (2019). Tissue fluidity promotes epithelial wound healing. Nat. Phys. *15*, 1195–1203.

Thompson, D.W.D. (1945). On growth and form (Cambridge university press).

Trepat, X., Wasserman, M.R., Angelini, T.E., Millet, E., Weitz, D.A., Butler, J.P., and Fredberg, J.J. (2009). Physical forces during collective cell migration. Nat. Phys. *5*, 426–430.

Tung, J.J., Tattersall, I.W., and Kitajewski, J. (2012). Tips, Stalks, Tubes: Notch-Mediated Cell Fate Determination and Mechanisms of Tubulogenesis during Angiogenesis. Cold Spring Harb. Perspect. Med. *2*, a006601–a006601.

Wetzel, G. (1926). Zur entwicklungsmechanischen Analyse des einfachen prismatischen Epithels. Wilhelm Roux Arch. Für Entwicklungsmechanik Der Org. *107*, 177–185.

Yang, R., Li, E., Kwon, Y.-J., Mani, M., and Beitel, G.J. (2019). QuBiT: a quantitative tool for analyzing epithelial tubes reveals unexpected patterns of organization in the Drosophila trachea. Development *146*, dev172759.

Yang, X., Bi, D., Czajkowski, M., Merkel, M., Manning, M.L., and Marchetti, M.C. (2017). Correlating cell shape and cellular stress in motile confluent tissues. Proc. Natl. Acad. Sci. *114*, 12663–12668.

bioRxiv preprint doi: https://doi.org/10.1101/2020.02.19.955567; this version posted June 21, 2020. The copyright holder for this preprint (which was not certified by peer review) is the author/funder, who has granted bioRxiv a license to display the preprint in perpetuity. It is made available under aCC-BY-NC-ND 4.0 International license.

bioRxiv preprint doi: https://doi.org/10.1101/2020.02.19.955567; this version posted June 21, 2020. The copyright holder for this preprint (which was not certified by peer review) is the author/funder, who has granted bioRxiv a license to display the preprint in perpetuity. It is made available under aCC-BY-NC-ND 4.0 International license.

Figure 1. Analysis of apico-basal cell intercalations in the Voronoi tubular model

A) Scutoids (left) entail apico-basal intercalations among packing cells that can be envisioned as *spatial* T1 transitions to exchange neighbors (right). The green and the red cells are neighbors in basal (but not in apical) while the opposite is true for the blue and the yellow cells. **B)** Voronoi *in silico* tubes with different surface ratios, s_b: $s_b = 2$ indigo blue; $s_b = 5$, dark blue (apical surface, light blue). **C)** For a given radial section (plane), cell boundaries emerge by applying a Voronoi tessellation to a number of seeds located in the plane. In the V1 (Voronoi 1) model seeds are randomly distributed. By applying iteratively the Lloyd algorithm (left to right) the topological disorder diminishes (**Materials and Methods**). **D)** The density plot shows the average number of apico-basal intercalations per cell in *in silico* tubes ($n = 20$) as a function of the surface ratio and the Voronoi class.

bioRxiv preprint doi: https://doi.org/10.1101/2020.02.19.955567; this version posted June 21, 2020. The copyright holder for this preprint (which was not certified by peer review) is the author/funder, who has granted bioRxiv a license to display the preprint in perpetuity. It is made available under aCC-BY-NC-ND 4.0 International license.

Figure 2. Three-dimensional packing and connectivity properties of the Voronoi tubular model

A) A schematic representation of a 3D histogram (density plot) where all cells have prismatic-like shapes (i.e., in the absence of scutoids). The histogram accounts for the probability that cells have n_a (number) of neighbors in the apical surface and n_b neighbors in the basal surface. If there are no scutoids, there are only contributions in the diagonal bins whereas if there are scutoids the distribution spreads away from the diagonal. **B)** 3D histograms of V5 tubes for increasing values of the surface ratio. The larger value of the spreading coefficient, η^2, (**Material and Methods**) indicates an increasing number of scutoids. **C)** and **D)** Density plots showing η^2 (**C**) and the average number of 3D neighbors, $\langle n_{3D} \rangle$, (**D**) as a function of the surface ratio and the Voronoi class in *in silico* tubes ($n = 20$).

bioRxiv preprint doi: https://doi.org/10.1101/2020.02.19.955567; this version posted June 21, 2020. The copyright holder for this preprint (which was not certified by peer review) is the author/funder, who has granted bioRxiv a license to display the preprint in perpetuity. It is made available under aCC-BY-NC-ND 4.0 International license.

Figure 3. Cells in the Voronoi tubular model follow a "poor get richer" principle

A) Average net gain of neighbors (density plot) with respect to the apical surface in Voronoi tubes with a surface ratio $s_b = 5$ as a function of the Voronoi class and the apical polygonal class ($n = 20$). Cells with a smaller polygonal class are more prone to gain neighbors. **B)** "Poor get richer" principle in V5 tubes with a surface ratio $s_b = 5$. The size of the circle accounts for the relative data count within each apical polygon class (numbers indicate the number of cells that gained 3D neighbors). The boxes indicate the $25\% - 75\%$ percentile interval, black lines the mean values, gray lines the standard deviation, and the red dotted lines the statistical median.

bioRxiv preprint doi: https://doi.org/10.1101/2020.02.19.955567; this version posted June 21, 2020. The copyright holder for this preprint (which was not certified by peer review) is the author/funder, who has granted bioRxiv a license to display the preprint in perpetuity. It is made available under aCC-BY-NC-ND 4.0 International license.

Box. In tubular geometries the 3D cellular connectivity gain decreases as the surface ratio increases and it is bounded. A) This panel shows, schematically, an apico-basal intercalation from the point of view of a Voronoi diagram and its topological dual, the Delaunay triangulation. Small solid circles indicate the seeds of Voronoi cells and large circles show the Delaunay property graphically: nearest neighbors define triangles (cells' seeds being their vertices) and circumscribed circles. For example, in the apical surface, the nearest neighbors of the red seed are those seeds at the circumscribed red circle. Likewise, the nearest neighbors of the green seed are those seeds in the green circle. Once the transition takes place, the seeds in each of the circles are nearest neighbors of the red and the green seeds. **B)** Before the apico-basal intercalation shown in **A)** occurs, the green seed is necessarily outside the circumscribed circle (otherwise it would be a nearest neighbor of the red seed). *Lemma 1* (**Materials and Methods**) states that if the green seed is going to become a nearest neighbor of the red seed due to an apico-basal transition then it is contained inside the parabola. As consequence of this, the 3D cellular connectivity gain decreases as the surface ratio increases: panels **C)**-**E)**. In this example, **C)**-**E)**, the Y axis represents the longitudinal axis of tubes, while the X axis accounts for the Cartesian projection of the transversal axis of radial sections. From left to right different radial sections are represented as s increases (as indicated by the color gradient arrow: from light to dark blue). In **C)** three Voronoi seeds that correspond to neighboring cells at the apical surface, $s = 1$, define the triangle ABC. Panels **D)** and **E)** track changes in the neighboring relations (accumulated neighbors) of cell A for two increasing values of s: 2 and 4.5 (panels **D)** and **E)** respectively). As shown in **C)**, should a new neighboring cell, D, of cell A appear due to an apico-basal intercalation, then its position must lie inside the vertical parabola defined by the points A, B and C, but outside the circle that these points define (white region), (*Lemma 1*). Regions accessible to new neighbors are then coded by the green shading in **C)**-**E)**. As s increases, see **D)**, and the cells A, B, C, and D become neighbors, then the parabolas and circles defined by ABD and ACD restrict the locations of future nearest neighbors. This idea is further reinforced in panel **E)**: winning neighbor E set additional limits to the

bioRxiv preprint doi: https://doi.org/10.1101/2020.02.19.955567; this version posted June 21, 2020. The copyright holder for this preprint (which was not certified by peer review) is the author/funder, who has granted bioRxiv a license to display the preprint in perpetuity. It is made available under aCC-BY-NC-ND 4.0 International license.

accessible locations of new neighbors. Thus, the potentiality of a connectivity gain by cell A due to apico-basal intercalations diminishes as the surface ratio increases and eventually becomes null: the number of 3D neighbors of a cell is bounded (**Materials and Methods**).

bioRxiv preprint doi: https://doi.org/10.1101/2020.02.19.955567; this version posted June 21, 2020. The copyright holder for this preprint (which was not certified by peer review) is the author/funder, who has granted bioRxiv a license to display the preprint in perpetuity. It is made available under aCC-BY-NC-ND 4.0 International license.

Figure 4. A probabilistic model reproduces the 3D cell connectivity behavior of epithelial tubes.

A) Top: in tubular geometries, cell intercalations along the apico-basal axis can be visualized as non-reversible spatial T1 transitions (once a neighbor is won it cannot be lost). Bottom: the "poor get richer" principle suggests an increasing energetic cost (i.e., a larger activation energy) for recruiting new 3D neighbors. In our model, β accounts for the energetic cost per 3D neighbor to recruit a new neighbor (**Materials and Methods**). **B)** The energy landscape shown in **A)** can be modeled by a stochastic dynamics (a Kolmogorov rate equation) where cells increase their 3D neighbors with a probability per unit of surface ratio, $r_{n,m}$, that depends on the activation energy and the maximum cell connectivity N_{max} (**Material and Methods**). **C)** Comparison between results obtained in the Kolmogorov model and simulations of V5 *in silico* tubes. The left/center density plots represent the connectivity distribution (i.e., the fraction of cells with a given number of 3D neighbors) as a function of the radial expansion obtained in the Voronoi simulation (left) and as predicted by the Kolmogorov model (center); the purple open circles (left/right) indicate the average number of 3D neighbors per cell $\langle n_{3D} \rangle$; the solid red line and the dashed white line (center/right) shows $\langle n_{3D} \rangle$ as obtained by the Kolmogorov model and the Flintstones' law respectively. The density plot on the right shows the difference between the predicted and the actual connectivity distributions and the corresponding error, ε^2 (magenta lines), see **Fig. S3** and **Material and Methods**.

bioRxiv preprint doi: https://doi.org/10.1101/2020.02.19.955567; this version posted June 21, 2020. The copyright holder for this preprint (which was not certified by peer review) is the author/funder, who has granted bioRxiv a license to display the preprint in perpetuity. It is made available under aCC-BY-NC-ND 4.0 International license.

Figure 5. Packing and connectivity analysis of *Drosophila's* salivary gland and comparison with the V8 model

A) Full projection of a salivary gland (cell contours stained by Cy3-labeled phalloidin, **Materials and Methods**). **B)** Computer representation of the segmented salivary gland shown in **A)** (**Material and Methods**). **C)** 3D rendering of a representative segmented salivary gland: apical surface, light green; basal surface, dark green. **D)** Density plots of the distribution of neighbor exchanges between apical and basal surfaces as a function of the number of neighbors in apical, n_a, and basal, n_b, surfaces (as in **Fig. 2B**): salivary glands (left) and V8 tubes (right) with surface ratio $s_b = 1.75$. **E**) Comparison between results obtained in salivary glands (top) and the simulations of the V8 model (bottom) in regards of the 3D cellular connectivity as a function of the surface ratio (see **Fig. 4C**).

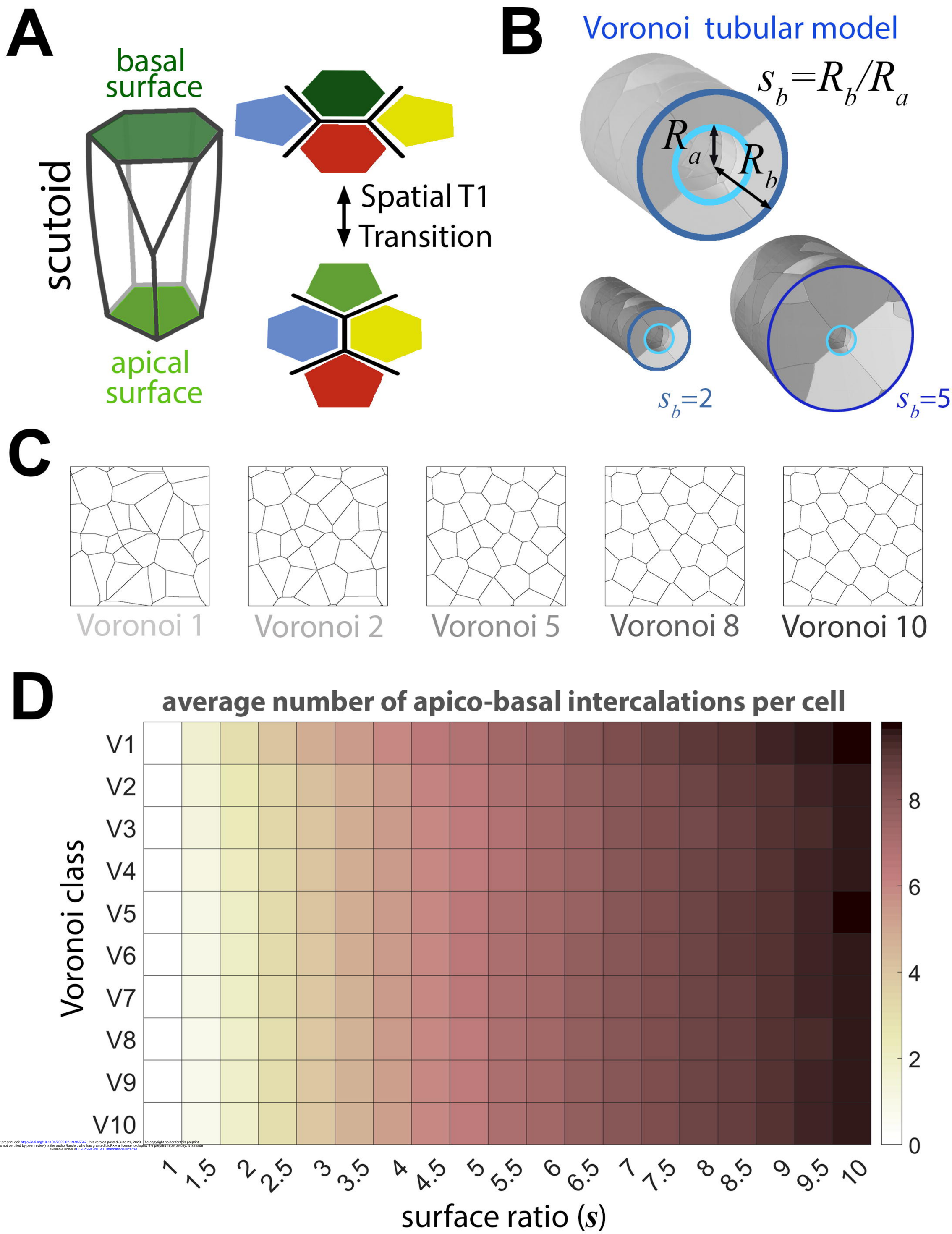

bioRxiv preprint doi: https://doi.org/10.1101/2020.02.19.955567; this version posted June 21, 2020. The copyright holder for this preprint (which was not certified by peer review) is the author/funder, who has granted bioRxiv a license to display the preprint in perpetuity. It is made available under aCC-BY-NC-ND 4.0 International license.

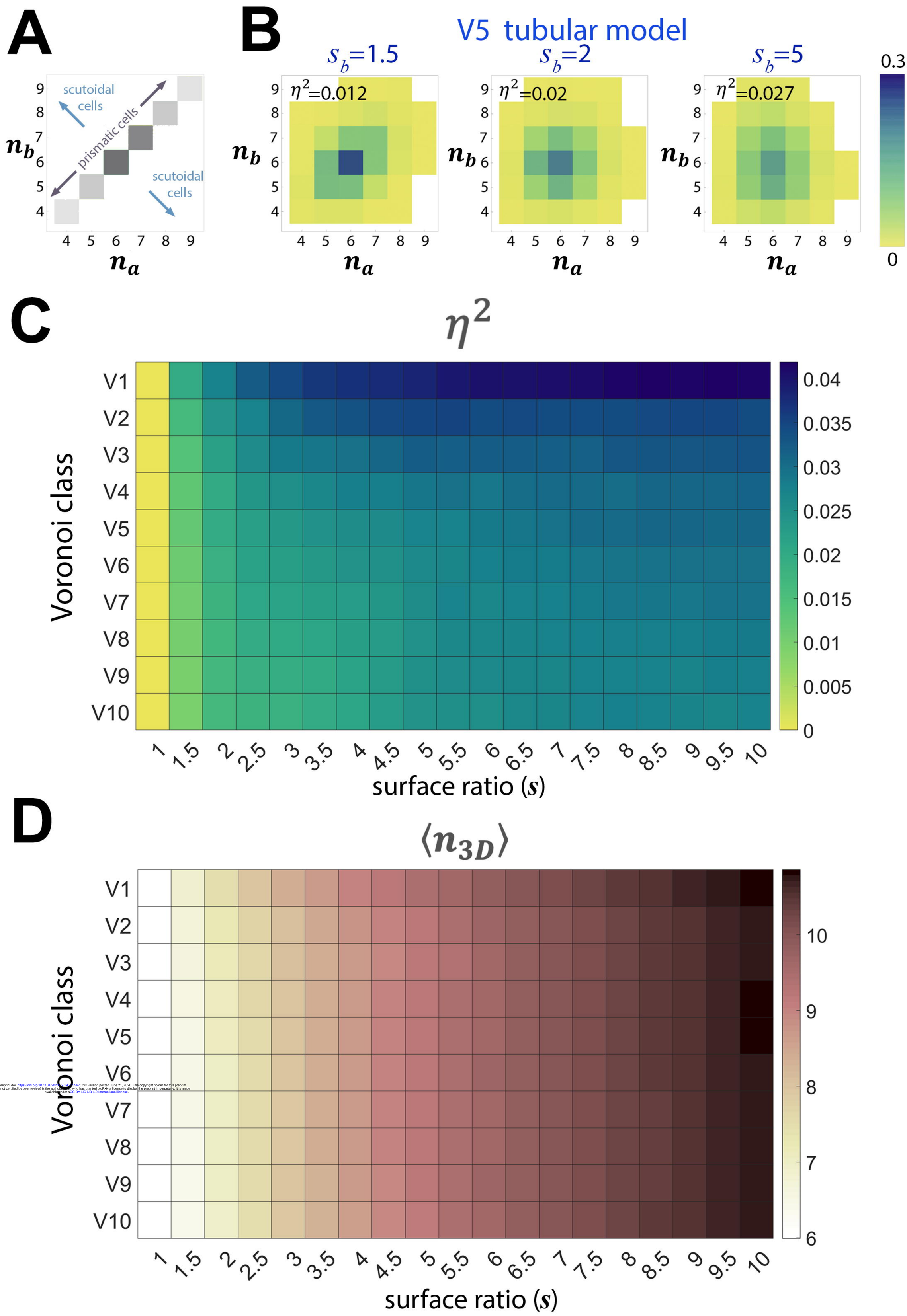

bioRxiv preprint doi: https://doi.org/10.1101/2020.06.19.165567; this version posted June 21, 2020. The copyright holder for this preprint (which was not certified by peer review) is the author/funder, who has granted bioRxiv a license to display the preprint in perpetuity. It is made available under aCC-BY-NC-ND 4.0 International license.

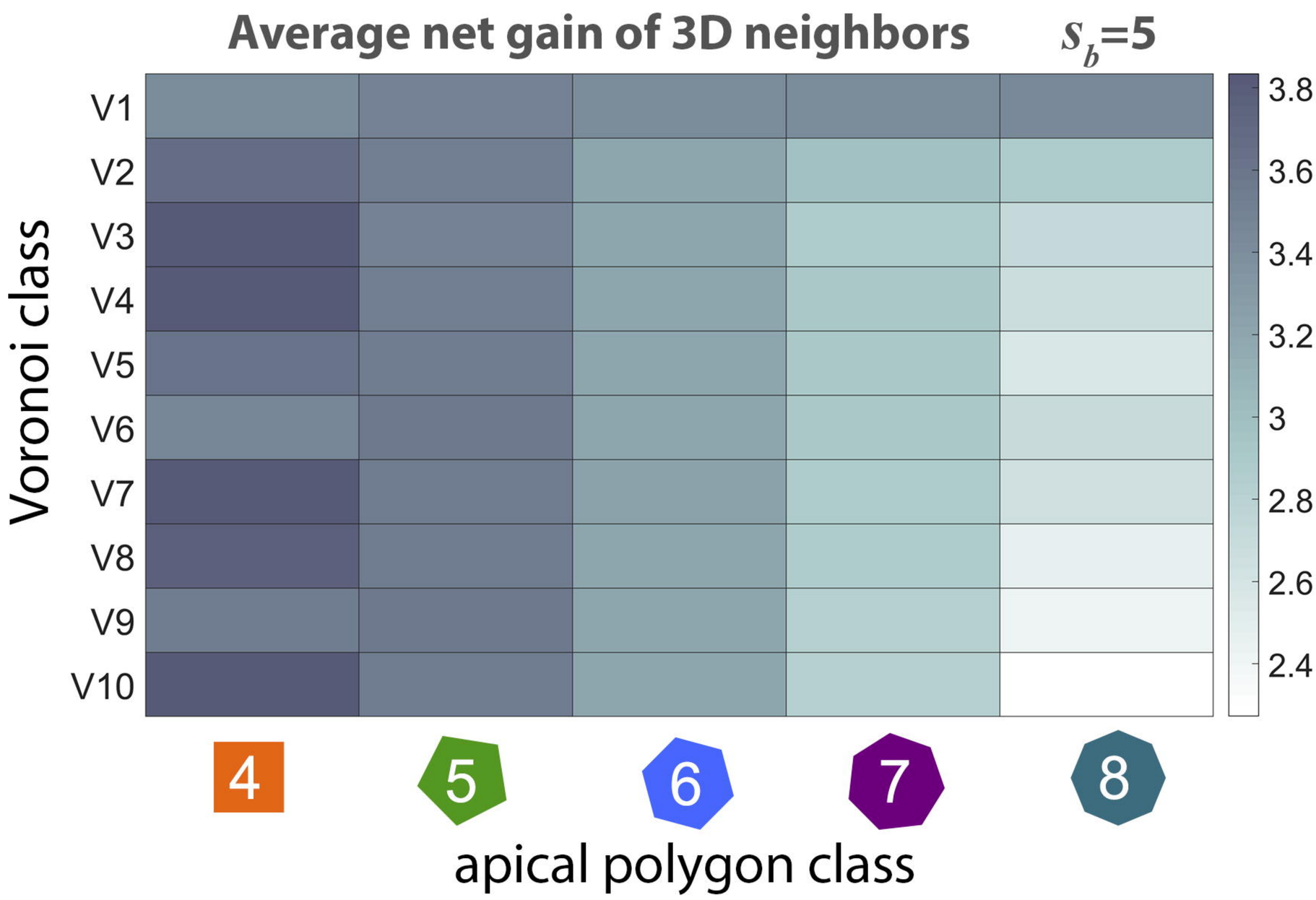

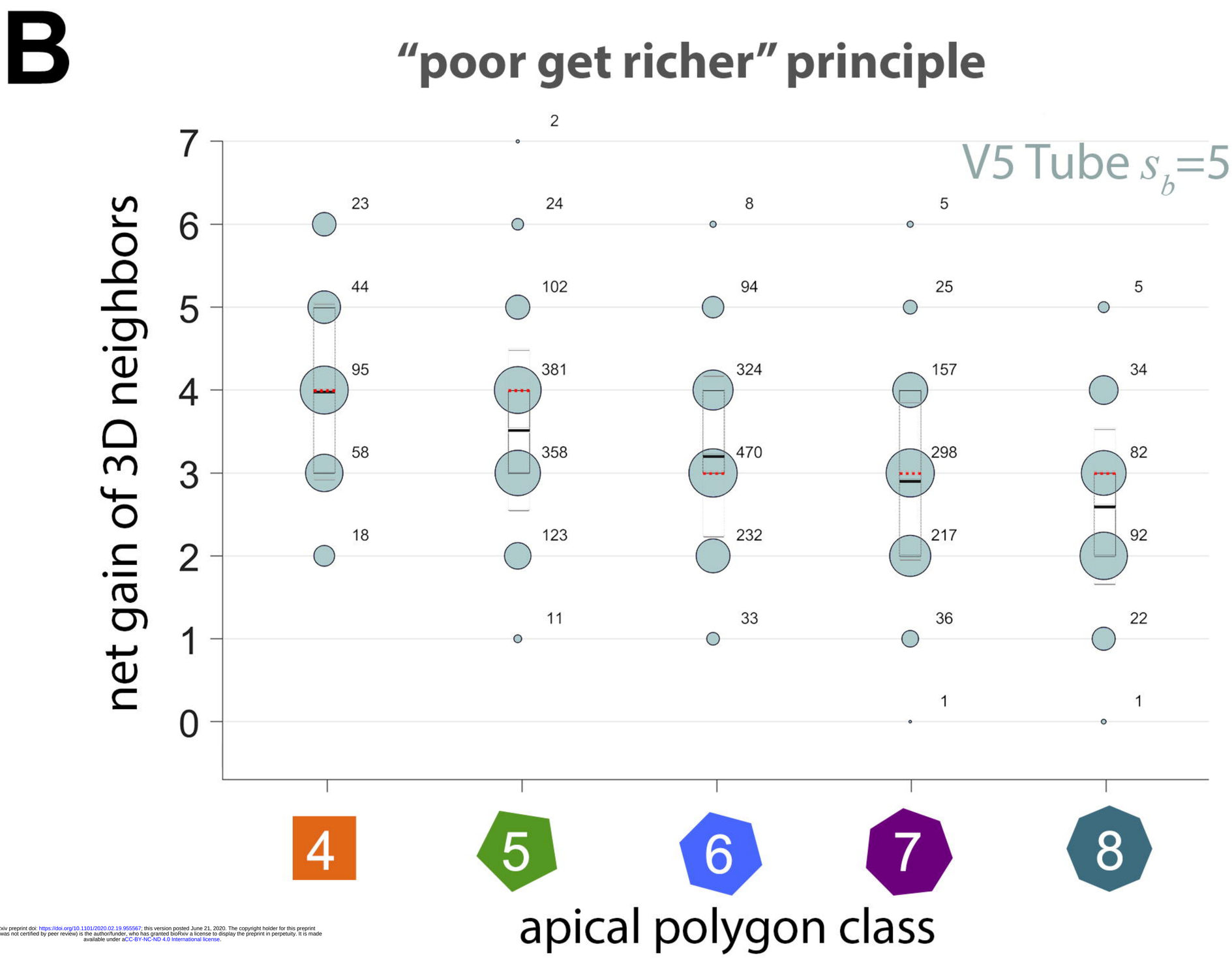

bioRxiv preprint doi: https://doi.org/10.1101/2020.02.19.955567; this version posted June 21, 2020. The copyright holder for this preprint (which was not certified by peer review) is the author/funder, who has granted bioRxiv a license to display the preprint in perpetuity. It is made available under aCC-BY-NC-ND 4.0 International license.

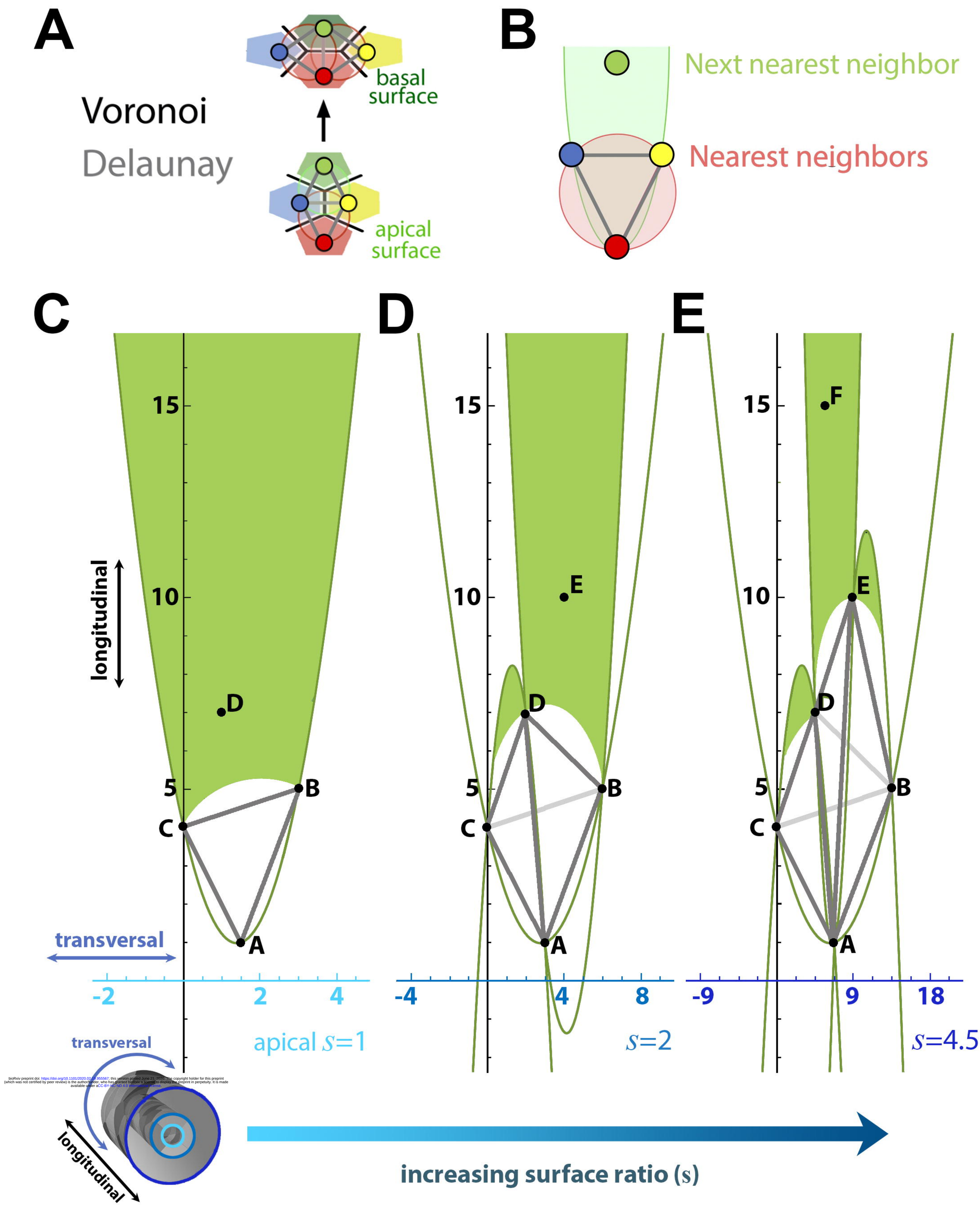

bioRxiv preprint doi: https://doi.org/10.1101/2020.02.19.955567; this version posted June 21, 2020. The copyright holder for this preprint (which was not certified by peer review) is the author/funder, who has granted bioRxiv a license to display the preprint in perpetuity. It is made available under aCC-BY-NC-ND 4.0 International license.

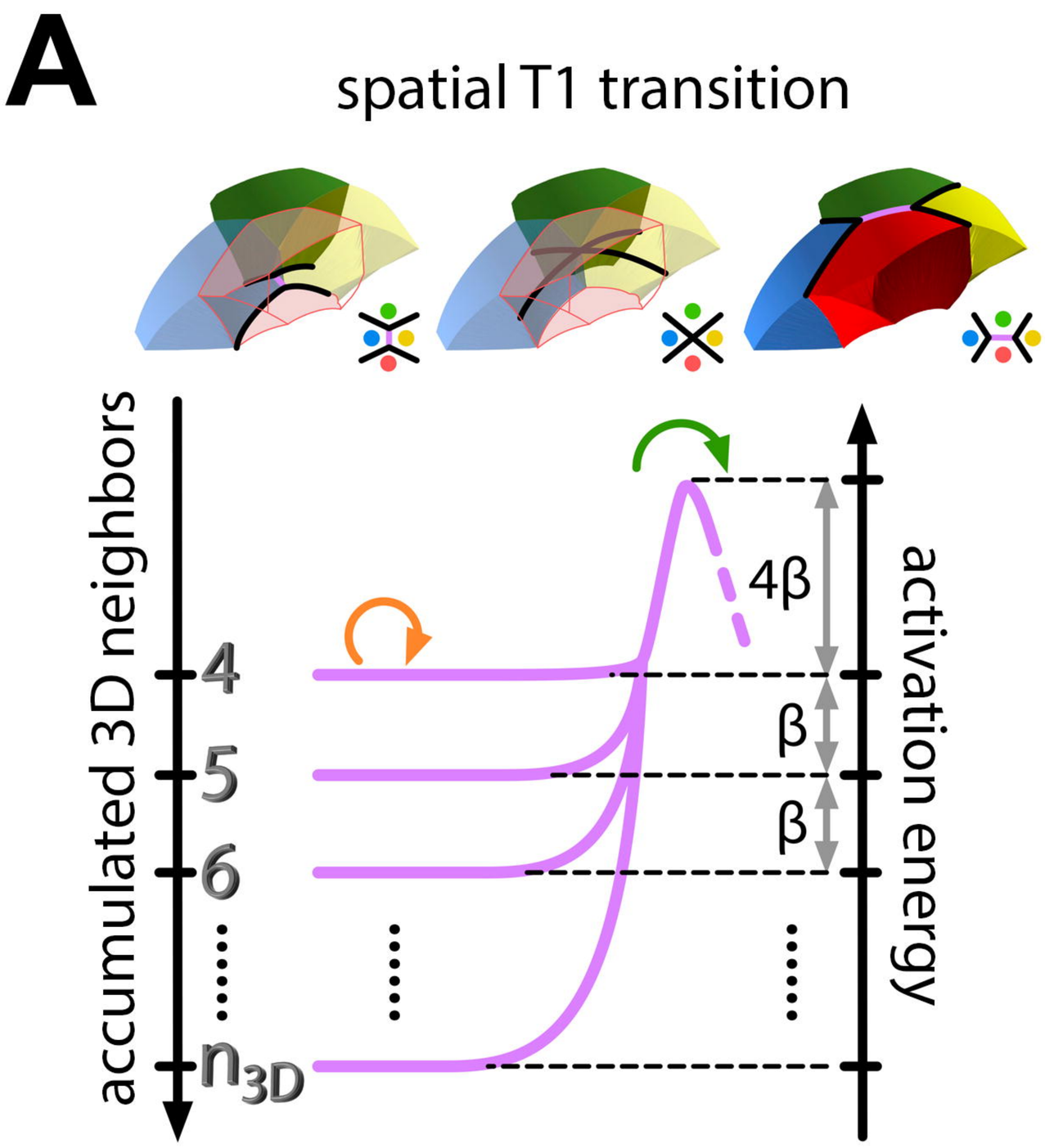

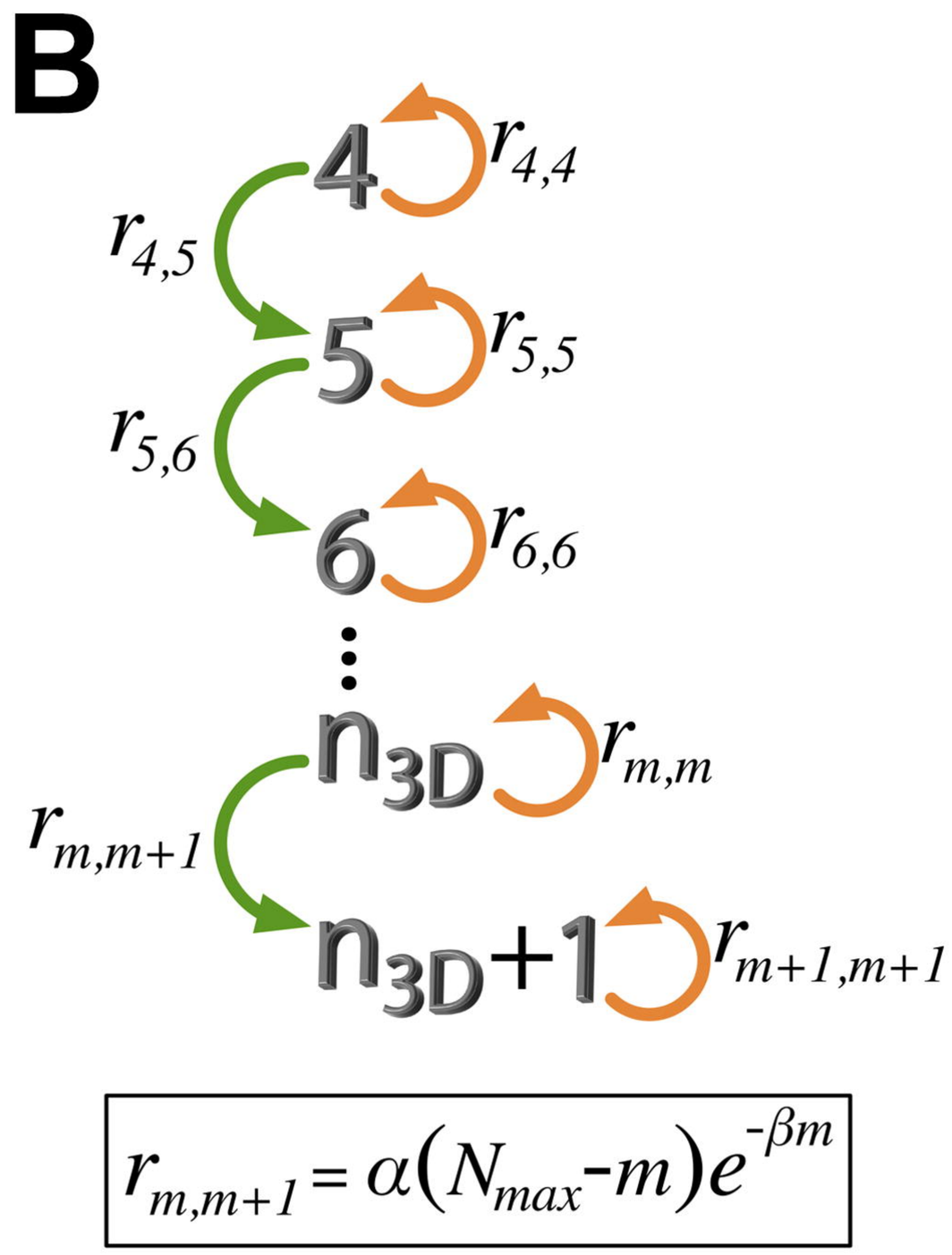

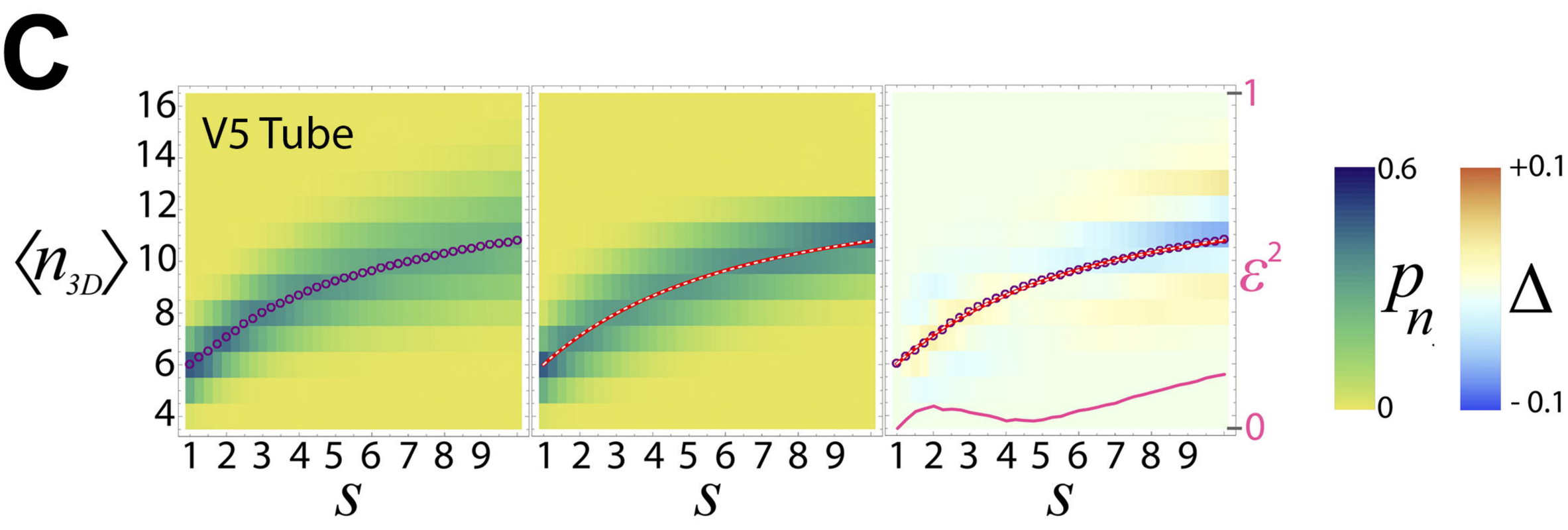

bioRxiv preprint doi: https://doi.org/10.1101/2020.02.19.955567; this version posted June 21, 2020. The copyright holder for this preprint (which was not certified by peer review) is the author/funder, who has granted bioRxiv a license to display the preprint in perpetuity. It is made available under aCC-BY-NC-ND 4.0 International license.

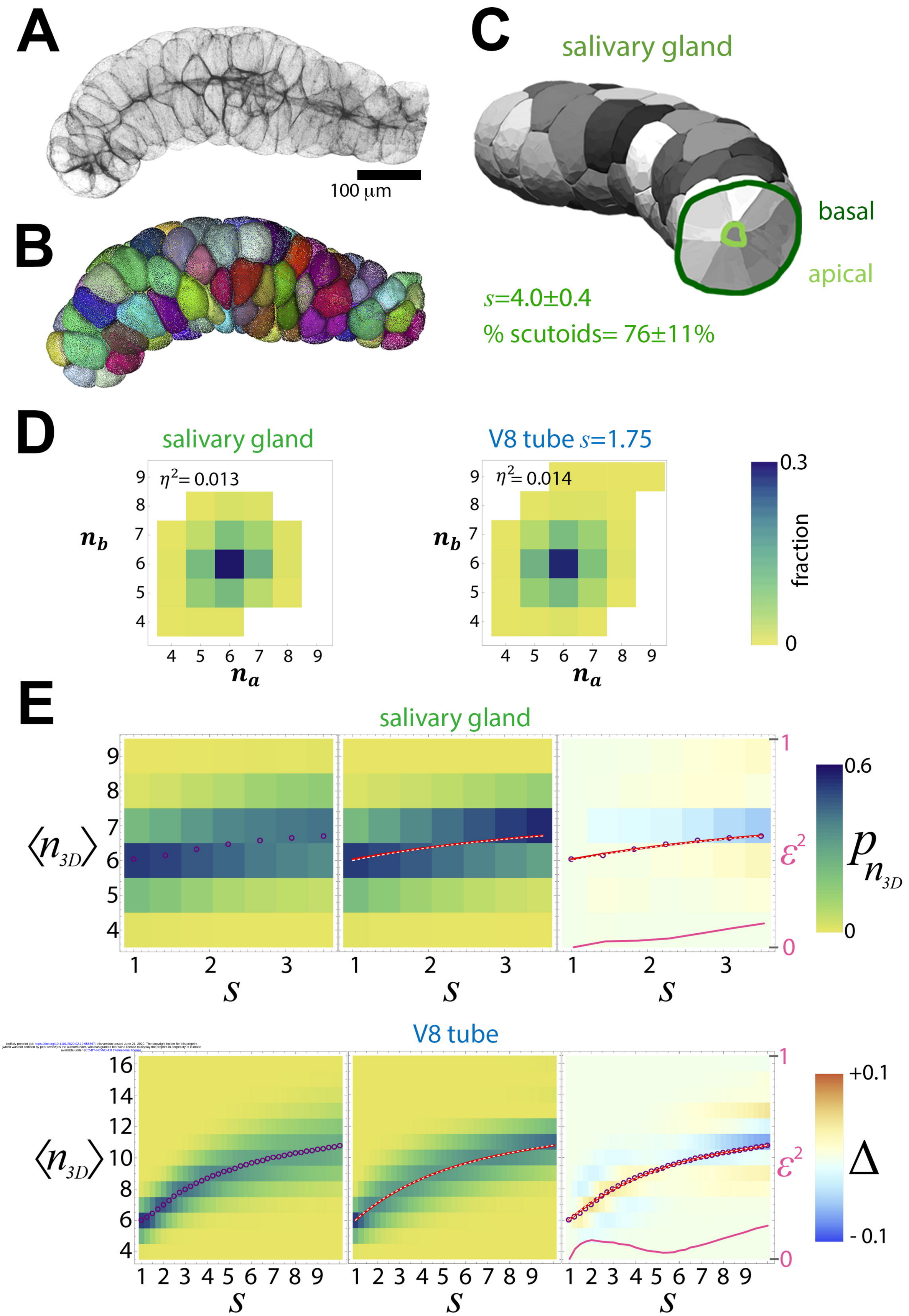

bioRxiv preprint doi: https://doi.org/10.1101/2020.02.19.955567; this version posted June 21, 2020. The copyright holder for this preprint (which was not certified by peer review) is the author/funder, who has granted bioRxiv a license to display the preprint in perpetuity. It is made available under aCC-BY-NC-ND 4.0 International license.